Cell Reports

Article

Probing multiplexed basal dendritic computations using two-photon 3D holographic uncaging

Graphical abstract

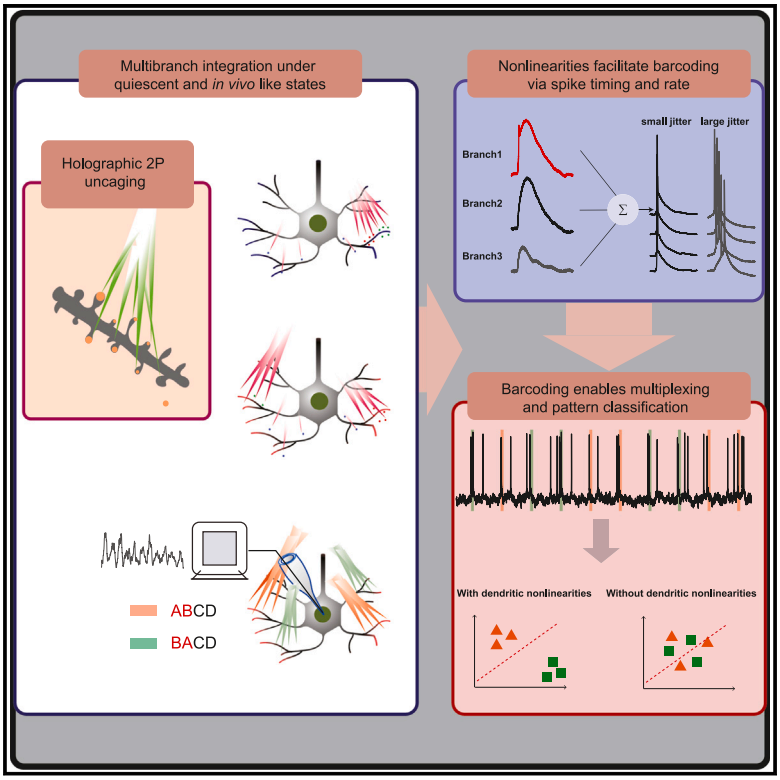

Authors

Shulan Xiao, Saumitra Yadav, Krishna Jayant

Correspondence

kjayant@purdue.edu

In brief

Xiao et al. use 3D two-photon holography, dynamic clamp, pharmacology, and modeling to unravel multibranch dendritic integration in layer 5 pyramidal neurons under quiescent and *in vivo*-like states. They reveal a critical role of dendritic nonlinearities in barcoding the somatic spike structure, allowing for optimal feature binding and pattern classification.

Highlights

- 3D two-photon holographic uncaging assays multibranch basal dendritic integration
- Dendritic nonlinearities facilitate barcoding via spike timing and rate modulation
- Barcoding enables multibranch multiplexing under quiescent and *in vivo*-like states
- Dendritic Na^+ spikes are critical for pattern classification

Xiao et al., 2024, Cell Reports *43*, 114413
July 23, 2024
https://doi.org/10.1016/j.celrep.2024.114413

CellPress

Cell Reports

CellPress
OPEN ACCESS

Article

Probing multiplexed basal dendritic computations using two-photon 3D holographic uncaging

Shulan Xiao,[1,3] Saumitra Yadav,[1,3] and Krishna Jayant[1,2,4,*]
[1]Weldon School of Biomedical Engineering, Purdue University, West Lafayette, IN, USA
[2]Purdue Institute for Integrative Neuroscience, Purdue University, West Lafayette, IN, USA
[3]These authors contributed equally
[4]Lead contact
*Correspondence: kjayant@purdue.edu
https://doi.org/10.1016/j.celrep.2024.114413

SUMMARY

Basal dendrites of layer 5 cortical pyramidal neurons exhibit Na^+ and *N*-methyl-D-aspartate receptor (NMDAR) regenerative spikes and are uniquely poised to influence somatic output. Nevertheless, due to technical limitations, how multibranch basal dendritic integration shapes and enables multiplexed barcoding of synaptic streams remains poorly mapped. Here, we combine 3D two-photon holographic transmitter uncaging, whole-cell dynamic clamp, and biophysical modeling to reveal how synchronously activated synapses (distributed and clustered) across multiple basal dendritic branches are multiplexed under quiescent and *in vivo*-like conditions. While dendritic regenerative Na^+ spikes promote millisecond somatic spike precision, distributed synaptic inputs and NMDAR spikes regulate gain. These concomitantly occurring dendritic nonlinearities enable multiplexed information transfer amid an ongoing noisy background, including under back-propagating voltage resets, by barcoding the axo-somatic spike structure. Our results unveil a multibranch dendritic integration framework in which dendritic nonlinearities are critical for multiplexing different spatial-temporal synaptic input patterns, enabling optimal feature binding.

INTRODUCTION

Cortical pyramidal neurons (PNs) in layer 5 (L5) respond with millisecond precision to sensory inputs.[1,2] Here, rapidly time-varying feedforward synaptic streams onto L5 basal dendrites modulate timing and gain of somatic action potentials (APs), creating a continuum in which precision and rate coding are embedded. Precise control of spike timing and rate is critical for neural coding and plasticity,[3,4] ensuring activation of apical calcium[5,6] and basal dendritic *N*-methyl-D-aspartate receptor (NMDAR)-dependent spikes,[7] and enabling calcium-activated burst mode signaling.[8] However, the stochastic nature of synaptic transmission, dendritic filtering, and high background conductance imply that signal integration and eventual AP generation will be variable. How L5 principal neurons reliably integrate and multiplex distinct feedforward synaptic input streams amid this stochastic background remains unknown.[9,10]

PNs receive excitatory inputs onto dendritic spines containing α-amino-3-hydroxy-5-methyl-4-isoxazolepropionic acid receptors (AMPARs) and NMDARs. While AMPARs mediate a fast-rising depolarization, NMDAR activation results in a slow current lasting ten to hundreds of milliseconds.[11] This slow NMDA-dependent current is crucial for synaptic amplification[12,13] and regenerating dendritic "plateau potentials" or NMDA spikes.[10,14–17] These nonlinearities also comprise dendritic Na^+ spikes, which can occur with or without an accompanying plateau potential, influencing sensory coding,[18] AP generation,[19] and plasticity.[20]

Basal dendrites of L5 PNs, which receive a diverse range of clustered feedforward[21] and intracortical synaptic inputs,[22–24] are uniquely poised to exert a potent influence on somatic action potential dynamics.[24–26] Synaptic clusters that promote regenerative spikes span 8- to 15-μm stretches and can be spread across multiple dendrites and interspersed alongside distributed inputs.[22,27–30] This regenerative property endows L5 PNs with an input-output transformation that follows the widely accepted two-layer model of computation,[31] which is highly location dependent across dendrites.[15,32] Furthermore, depolarization reduces the NMDA spike threshold, making the generation of NMDA spikes dependent not only on the efficiency of glutamate binding but also on the cooperativity between different dendritic integration phenomena.[17,26,33,34] These phenomena include previous regenerative events, nonlinearities that spread across dendritic branches, or invading back-propagating APs.[35,36] These nonlinearities occur alongside linear/sublinear integration of sparse synaptic inputs correlated in time.[10] It is not yet fully understood how the soma reliably encodes synaptic activation patterns in light of this mixed integration framework. While evidence suggests that dendritic spikes can co-exist simultaneously across multiple branches, including exhibiting a mixture of Na^+ and NMDA spikes,[37] it remains unclear whether the axo-somatic spike structure can help barcode the synaptic patterns that caused them.

Neurons exhibit elevated conductance and noisy backgrounds *in vivo*.[38] This background noise consists of sharp

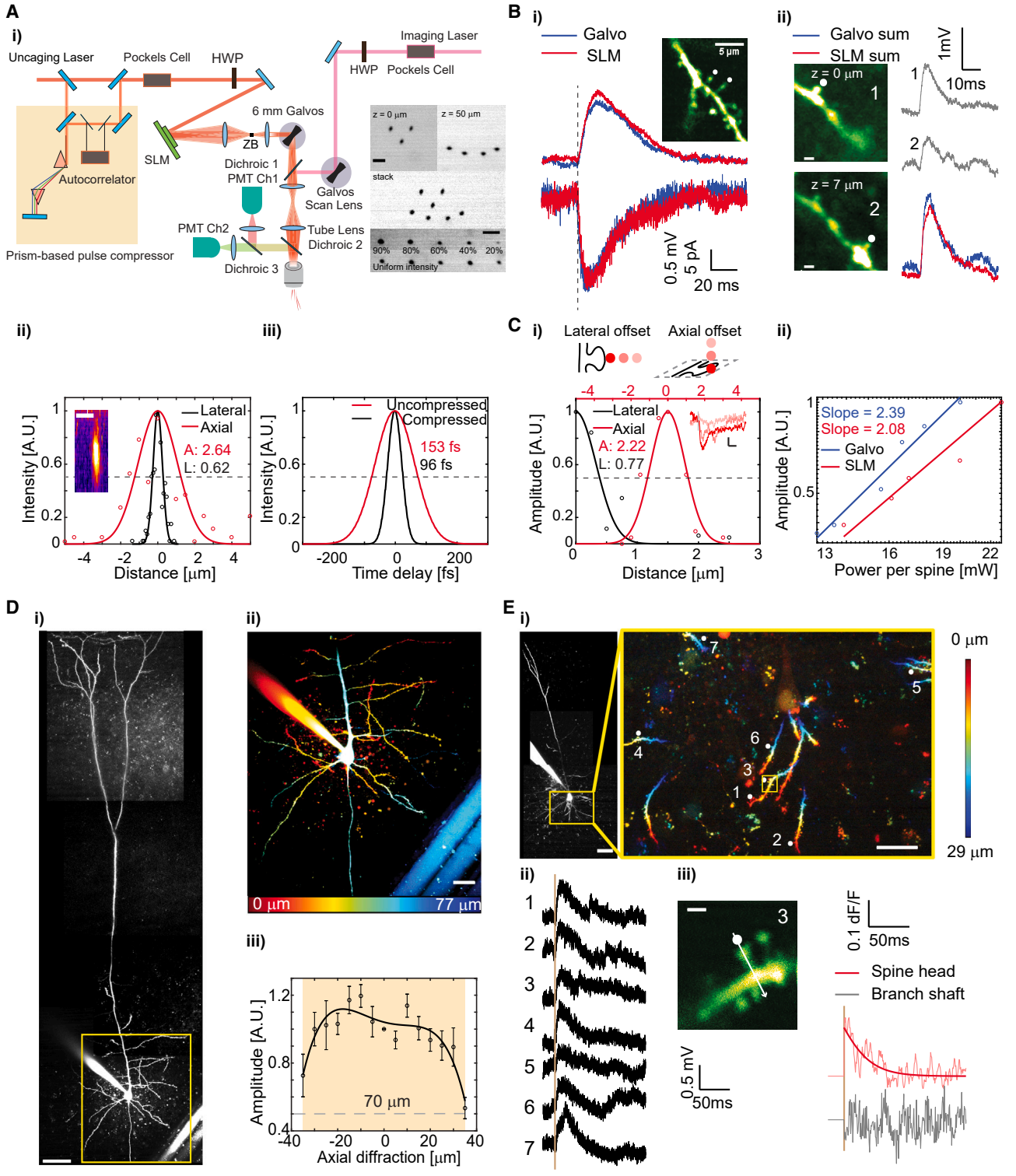

Figure 1. 3D two-photon spatial light modulator (SLM)-based uncaging

(A) (i) The two-photon microscope with imaging and uncaging paths. (Right inset) A 3D holographic pattern (top) and independent power weighting of holographic spots (bottom). Scale bars, 5 µm. (ii) Holographic uncaging point spread function (PSF). (Inset) x-z projection of a 100-nm fluorescent bead imaged with a holographic beamlet. Scale bars, 2 µm. (iii) Holographic uncaging pulse width, with and without pulse compression.

(legend continued on next page)

voltage fluctuations, which is shown to reduce spike jitter and improve AP precision.[18,38–42] Dendrites, with their unique morphology, varied resistance, and a myriad of nonlinear regenerative transformations, are believed to be a locus of such sharp fluctuations and play a key role in determining accurate AP generation. However, the interplay between synaptic input patterns, widespread dendritic regenerative events, and noisy background conductances, critical to understanding feature selectivity and binding, has remained experimentally intractable.[9,43,44] For example, is there a critical number of synaptic inputs that must be co-active to impact AP output under *in vivo*-like conditions? Do back-propagating spikes reduce the efficacy of synaptic cluster-evoked somatic control and eventual multiplexing? Unraveling multibranch dendritic integration under quiescence conditions and increased background conductance will allow us to address these outstanding questions.

Previous reports focusing on assaying the role of multisite/multibranch dendritic inputs used multisite focal theta stimulation,[45] acousto-optic deflector (AOD)-based uncaging,[46] and single-photon[47,48] or two-photon holographic uncaging[49,50] with phase-only spatial-light modulators (SLMs). While multisite theta stimulations assist in generating dendritic spikes, the ability to precisely stimulate clusters and distributed inputs in synchrony and across space is impossible. AODs, on the other hand, offer higher positioning speeds but suffer from spatiotemporal distortion of ultrafast laser pulses and exhibit a wavelength-dependent low diffraction efficiency, leading to small fields of view and precluding simultaneous 3D uncaging to date.[46] Two-photon uncaging of transmitters using a set of galvanometers allows for precise stimulation of individual and synaptic clusters, respectively,[13,15,16,20,51] wherein galvanometric mirrors can be programmed to allow for fast beam steering and rapid repositioning (~100 μs) with little to no power loss. However, they are limited to a single focal plane and cannot assay 3D synaptic distributions.[52] While single-photon holographic uncaging suffers from poor point-spread functions (PSFs),[47] two-photon holographic uncaging promises to overcome these limitations, yet previous efforts have fallen short of experimental demonstrations of the full 3D capability.[49,50]

We combine an SLM with custom-built table-top pulse compression optics into a conventional two-photon microscope to enable 3D caged-transmitter uncaging in thick scattering tissue. We integrate this holographic uncaging approach with whole-cell electrophysiology, dynamic clamp, and computational modeling to elucidate the mechanisms underlying multiplexed barcoding of synaptic input streams under quiescence and *in vivo*-like conditions. Our recordings reveal that precise AP timing and AP burst control under synchronous synaptic streams, mediated by Na^+ and NMDA spikes spread across multiple basal dendritic branches, are critical to barcoding synaptic streams, which enables multiplexing through distinct spike structures amid an ongoing background.

RESULTS

3D two-photon holographic uncaging: Characterization

Our system comprises a commercial two-photon microscope integrated with an SLM module, custom-designed table-top compression optics, a Michelson interferometer, and dual laser lines for simultaneous imaging and uncaging (Figure 1Ai). The setup is capable of 3D stimulation (Figure 1Ai, inset, top) with power weighting for each point independently (Figure 1Ai, inset, bottom, see STAR Methods). The PSF of our SLM-based system (0.6 μm lateral, 2.5 μm axial, Figure 1Aii) measured using 100-nm fluorescent beads was found to be identical to that with just galvanometric mirrors (Figure S1A). While the lateral PSF aligns with previous experimental measures,[53] the axial PSF was slightly higher than previously reported values (~1.3–2 μm axial).[54–56] We attribute our slightly higher axial PSF to the marginally underfilled objective (0.8 NA) in our design, which is critical to maximizing power transmission by the SLM. This ensures an optimal tradeoff between power per spine and a desired resolution. The combined use of the SLM and galvanometric mirrors allowed us to reposition the holographic fields of view (FOVs) rapidly (Figure S1B) while ensuring diffraction-limited synaptic stimulation in 3D with a desired number of beamlets. The use of a custom-designed prism-based compressor allowed us to achieve sub-100-fs pulse widths at the sample plane for efficient SLM-based uncaging (Figure 1Aiii), albeit slightly higher than for galvanometric scanning (Figure S1C).

Next, we measured the physiological PSF of SLM-based uncaging and compared it with galvanometric uncaging. We found that glutamate uncaging responses (1.5 mM DNI-glu; 1-ms pulses; see STAR Methods) with both the SLM and galvanometric mirrors on two spines located in the same plane and two different planes separated by 7 μm were identical (Figure 1B). Galvanometric uncaging was independently performed at both focal planes and compared to the holographic uncaging response. The physiological PSF of the SLM (Figure 1Ci) was found to be indistinguishable from the measures using beads (Figure 1Aii) and resulted in the same excitatory postsynaptic potential (EPSP) and excitatory postsynaptic current (EPSC) kinetics and amplitudes in comparison to galvanometric scanning (Figures S1D and S1E). The power needed to evoke a unitary

(B) Holographic vs. galvanometric uncaging efficiency. (i) EPSPs and EPSCs induced by galvanometric (blue) and holographic (red) uncaging across two spines (dashed line: time of uncaging event). Scale bar, 5 μm. (ii) Holographic uncaging-evoked EPSP of two spines across different depths (red), compared to the linear sum (blue) of the individual EPSPs (gray) from each spine under galvanometric uncaging. Scale bars, 1 μm.

(C) (i) Physiological holographic uncaging PSF measured as the normalized amplitude of EPSP/EPSC under lateral (black) and axial (red) offsets from the spine head. Inset: EPSCs evoked by laterally offsetting the holographic spot from the spine head (0, 0.25, 0.5 μm). Scale bars, 5 ms (horizontal) and 5 pA (vertical). (ii) EPSP amplitudes as a function of galvanometric (blue) and SLM (red) uncaging laser power.

(D) Uniform holographic uncaging efficiency across depth. (i) An example L5 pyramidal neuron. Scale bar, 50 μm. (ii) Basal dendrites distributed across ~70 μm of depth. Scale bar, 20 μm. (iii) EPSP amplitudes as a function of axially diffracting the holographic uncaging beamlet, $n = 3$ cells (full width at half maximum ~70 μm, shaded window).

(E) (i) An example L5 pyramidal neuron and magnified view of the basal dendrites. Scale bars, 50 μm (main) and 20 μm (inset). (ii) Scanless single-spine EPSPs from seven spatially distributed basal dendritic spines. (iii) A Ca^{2+} line-scan across spine no. 3 (yellow square in i). Scale bars, 1 μm.

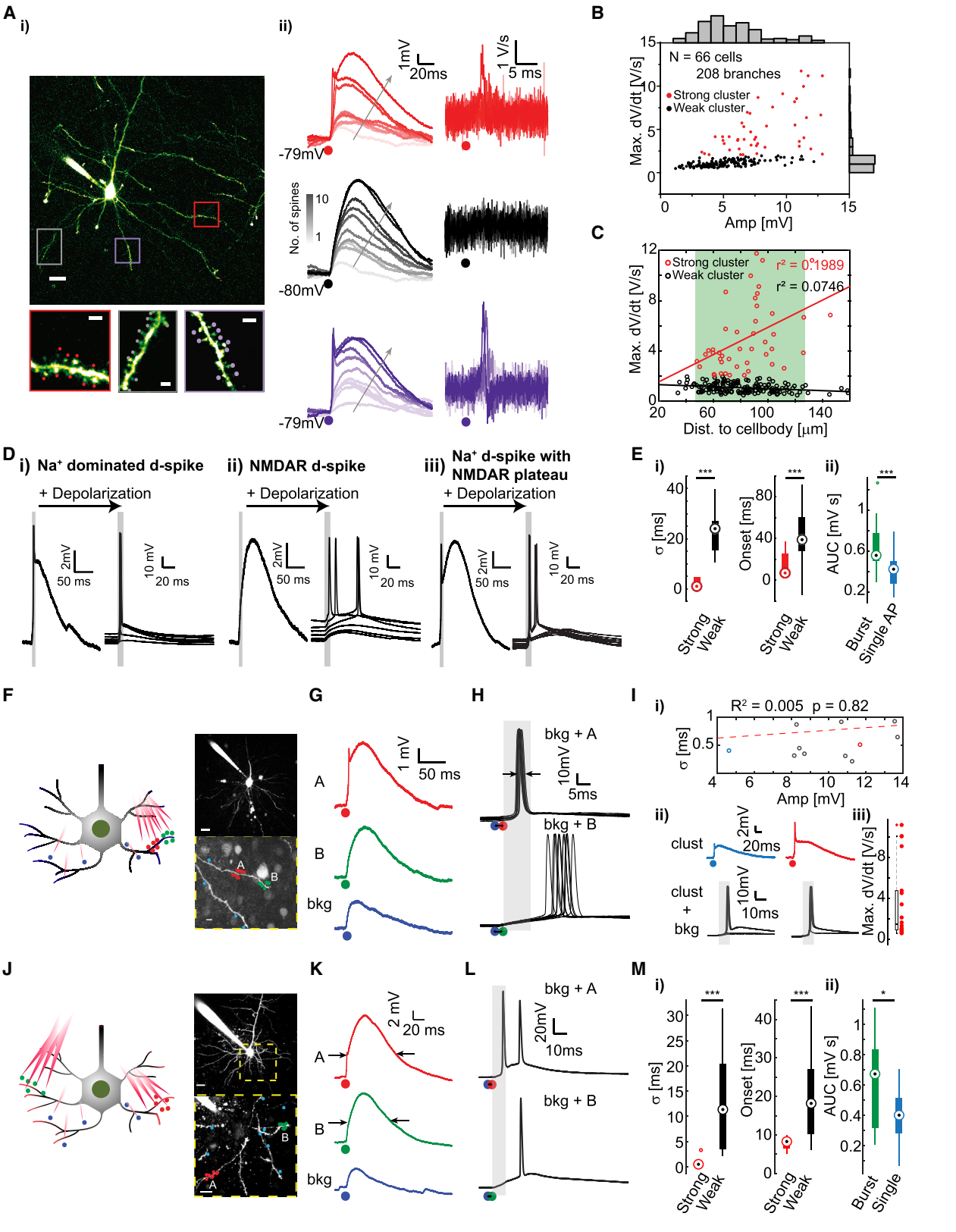

(legend on next page)

response (~0.5 mV) from a single spine with the SLM engaged was 15–17mW with pulse compression (Figure 1Cii), and this was only slightly higher than the power needed for uncaging with galvanometric mirrors. Pulse compression did not change the physiological PSF (Figure S1F). This ensured stimulation of spines with no observable photodamage even after repeated stimulations (Figure S1G; also see STAR Methods).

L5 pyramidal neuron basal dendrites are distributed across a depth of ~50 μm (Figure 1Di, ii). Since the diffraction efficiency of the SLM decreases with increasing angle of beam steering, we calibrated the axial limits of the SLM before an appreciable power roll-off (see STAR Methods). The amplitude of spine-evoked EPSPs measured at the soma remained identical across an axial range of ±35μm (Figure 1Diii), resulting in a uniform uncaging FOV across a 70-μm depth, which largely covers the L5 PN basal dendritic arborization in acute brain slices. We then performed scanless holographic uncaging across several spines spread across diametrically opposite basal arbors encompassing a 100 μm × 100 μm × 35 μm FOV and found that each synapse was uncaged with similar efficiency and specificity (Figure 1Ei, ii). Critically, calcium imaging across a chosen spine reflected compartmentalized calcium signaling restricted to the spine head and not the dendritic shaft (Figure 1Eiii), suggesting minimal to no off-target activation. However, when clusters of synapses were activated, calcium signals in dendrites reflected the cooperativity across clustered inputs (Figure S1H).

Dendritic nonlinearities dictate somatic spike timing and gain

Basal dendrites of L5 PNs exhibit a rich repertoire of local nonlinearities and have a high input impedance and large space constant.[37] A key component underlying these nonlinearities is clusters of co-active, closely spaced synapses, which, via NMDAR cooperativity, lead to local dendritic spikes (d-spikes). Using 3D two-photon holographic uncaging of synaptic clusters across multiple basal dendrites of a single L5 pyramidal neuron, we observed distinct nonlinear input-output transformations as a function of number of synapses stimulated simultaneously (Figure 2A), characteristic of a sigmoidal input-output pattern (Figures S2A and S2B). Here, cells were hyperpolarized from rest to reveal the full length of the nonlinear d-spike without evoking a somatic AP. While some basal dendritic clusters exhibited a fast-rising Na^+ spike characterized by a high dV/dt followed by a large NMDAR-dependent plateau (Figure 2A, red and magenta) (strong cluster, classified based on maximum dV/dt), several clusters revealed a purely NMDAR-dependent signal (Figure 2A, black) (weak cluster). The NMDAR plateau potential was found to be dependent on D-(-)-2-amino-5-phosphonopentanoic acid (AP5) (Figures S2C–S2E), while the Na^+ spike was critically dependent on tetrodotoxin (TTX) (Figures S2F–S2G). Note that even in the strong clusters, NMDAR plays a role in promoting the nonlinearities and boosting the dendritic Na^+ spike formation, as blocking Na^+ channels with TTX does not fully remove the dendritic nonlinearity, but subsequent application of AP5 abolishes the nonlinearity (Figure S2H). Na^+ spikes characterized by the fast dV/dt component showed a weak trend with respect to overall d-spike amplitude (Figure 2B) as well as a location dependence along the basal dendrites, occurring between 50 μm and 150 μm away from the soma (Figure 2C). To investigate the effects of dendritic spikes on somatic APs, we then slowly ramped the resting membrane potential (RMP) of the cell via the patch electrode and observed that when the RMP was close to the threshold, dendritic nonlinearities exhibiting the fast Na^+ spike resulted in a precise AP output with millisecond precision and very low jitter (Figure 2Di). However, d-spikes reflecting pure NMDAR events (weak cluster) led to AP output with much larger variability and high jitter (Figure 2Dii). Importantly, a subset of Na^+ d-spikes followed by large NMDAR plateaus resulted in precise bursts of APs with very low jitter (Figure 2Diii). In comparison, NMDAR events alone exhibited a large jitter, i.e., standard deviation of spike timing and variable onset (Figure 2Ei). However, large plateau potential (quantified with

Figure 2. Dendritic nonlinearities regulate timing and gain of somatic action potentials

(A) (i) An L5 pyramidal neuron (scale bar, 20 μm) and three basal dendritic segments (scale bars, 2 μm) with clustered synapses. (ii) Holographic uncaging-evoked potentials (left) and corresponding dV/dt (right) while gradually increasing the number of co-active spines within each cluster.

(B) Maximum dV/dt vs. amplitude of uncaging-evoked d-spikes. Red dots, "strong" clusters that evoke Na^+ d-spikes; black dots, "weak" clusters that evoke plateau potentials without Na^+ spikelet.

(C) Maximum dV/dt of the uncaging-evoked d-spikes as a function of distance between the cluster and cell body. Red circles, strong clusters; shaded zone, the putative Na^+-rich zone. n = 208 clusters from 66 cells for (B) and (C).

(D) (i–iii) Synaptic cluster uncaging-evoked responses as a function of somatic depolarization (shaded zone: 10-ms window after the uncaging onset) reveal distinct spike structures under different types of d-spikes.

(E) (i) Uncaging of strong clusters under depolarization evoke APs with smaller jitter (σ) and shorter onset delay (Mann-Whitney-Wilcoxon test, n = 14 strong and 28 weak clusters from 20 cells, $p < 0.001$). (ii) Area under the curve (AUC) of the cluster-evoked plateau potentials correlates with burst generation (Mann-Whitney-Wilcoxon test, n = 11 burst-evoking and 31 single-AP-evoking clusters from 20 cells, $p < 0.005$).

(F) Experimental arrangement depicting co-activation of clustered and distributed spines. Scale bars, 20 μm (top) and 5 μm (bottom).

(G) Holographic uncaging-evoked potentials across a strong cluster (A, red), a weak cluster (B, green), and a set of spatially distributed synapses (bkg, blue).

(H) Somatic spikes (ten repetitive trials) upon holographic co-activation of A + bkg and B + bkg.

(I) (i) No correlation between Na^+ d-spike amplitude and spike jitter observed (R^2 = 0.005, n = 11 strong clusters from 9 cells, p = 0.82). (ii) Precise APs are evoked by both large (red) and small (blue) Na^+ d-spike amplitudes, respectively. (iii) Maximum dV/dt of the clusters that lead to precision (jitter < 1 ms).

(J) Clusters are evoked on different basal dendrites with distributed background spines. Scale bars, 20 μm (top) and 10 μm (bottom).

(K) Holographic uncaging response of a cluster evoking a broader plateau potential (A), a cluster with narrower potential (B), and the background synapses (bkg).

(L) The somatic spikes evoked by A and B co-activated with background synapses, respectively.

(M) (i) Strong clusters lead to less somatic spike jitter and faster spike onset when co-activated with distributed background (Mann-Whitney-Wilcoxon test, n = 12 strong clusters and 20 weak clusters across 25 cells, $p < 0.001$). (ii) Burst-generating clusters show a larger d-spike AUC (Mann-Whitney-Wilcoxon test, n = 13 bursts-evoking and 19 single-AP-evoking clusters from 25 cells, $p < 0.05$).

the area under the curve [AUC]) shows a higher propensity to evoke somatic bursts of APs (Figure 2Eii). The results shown in Figures 2A–2E suggest that while spike timing critically depends on Na^+ d-spikes, NMDAR spikes lead to variable jitter but higher gain, and both influence AP output.

Next, since distributed synaptic inputs sum sublinearly at the cell body and do not affect the Na^+ or NMDA d-spike features (Figure S3), we co-activated spatially distributed and clustered synapses to unravel this relationship. We first performed 3D holographic uncaging across two synaptic clusters while simultaneously stimulating a distributed synaptic input pattern across multiple dendritic arbors (Figure 2F). The neuron at rest fluctuated between an approximate RMP of −65 mV to −62 mV, and no current was injected to maintain this RMP. While one strong cluster (denoted A) showed a distinct Na^+ spike followed by a plateau, a second weak cluster revealed a plateau reflective of an NMDAR event but without the Na^+ component (denoted B) (Figure 2G). The distributed input (denoted bkg for background) resulted in a small amplitude (∼2–5 mV) yet slowly varying depolarization, which was insufficient to drive somatic spiking. While cluster A paired with the distributed background resulted in precise AP generation, cluster B paired with the distributed background resulted in a highly jittered AP response (Figure 2H), similar to when the RMP was modulated by current injection via the patch pipette (Figure 2Di, ii). Significantly, and in line with the results from Figure 2B, both low- and high-amplitude Na^+ d-spikes resulted in millisecond AP timing (Figure 2Ii), suggesting that amplitude of the d-spike (Figure 2Iii) was not a critical determining factor in ensuring precision but rather the maximum dV/dt. Importantly, we found that even small dV/dt values (∼2 V/s) were sufficient to generate precise spikes (Figure 2Iiii), in agreement with earlier reports from CA1 cells.[19,20]

Since temporal precision was not dependent on d-spike amplitude or the total amount of axial charge prior to spike onset (Figure S4A), but rather dependent on the maximum dV/dt, precision evoked by dendritic Na^+ spikes could not be explained with a fixed AP threshold. Previous experimental reports have suggested that precise APs occur when the stimulus is dynamic, time-varying, and noisy instead of quasi-static.[41] In particular, the frequency content of the stimulus impacts spike precision.[57] While dendritic Na^+ spikes reflect a fast fluctuation with high-frequency content, they could be an ideal substrate to gate axo-somatic channels in a stochastic manner, enabling efficient AP generation. To reveal the role of stochastic gating by Na^+ spikes, we numerically simulated the probabilistic description of Hodgkin-Huxley style ion channels[58,59] (Figure S4B). We injected the experimentally measured cluster-evoked dendritic spike waveform as axial current to the stochastic Hodgkin-Huxley model. The Na^+ spikelet evokes high-precision somatic APs, while NMDAR events show an appreciable jitter (Figure S4C). This simulation result verified that the time course of dendritic Na^+ spike is sufficient for enhancing AP precision via stochastic gating.

However, the Na^+ spikelet alone does not explain the burst regulation, since both bursts and single AP could be equally evoked by strong clusters (Figures S5A–S5E). Notably, these short bursts (doublets and triplets) could be evoked purely with basal synaptic drives without evoking an apical Ca^{2+} plateau (Figures S5F and S5G), making it possible for feedforward inputs to be frequency-division multiplexed. Since the AUC of the d-spike waveform is correlated with burst generation (Figure 2Eii), we investigated whether the d-spike plateau mediates the burst propensity. When two clusters on separate basal dendritic branches were paired with a distributed background (Figure 2J), the cluster with a larger plateau (denoted A, Figure 2K) evokes a somatic burst (Figure 2L). The smaller plateau (denoted B) evokes only a single AP. Together, the above results highlight three critical features. First, dendritic Na^+ spikes control somatic spike precision irrespective of background inputs. Second, NMDAR spikes lacking the Na^+ component but large enough to depolarize the soma above threshold results in a variable spike onset (Figure 2Mi). Finally, the size of the dendritic plateau is critical in determining burst propensity (Figure 2Mii). Noteworthily, despite the known difference in morphology, connectivity, and electrical properties, both subtypes of L5 PNs (L5a and L5b PNs) show Na^+ spikelet-mediated precision control with basal dendritic activation. Still, only putative L5b PNs generated bursts (Figure S6). This suggests a possible universal time-coding strategy adapted by both subtypes of L5 PNs.

Multibranch and multicluster control of somatic spiking output

To verify whether the temporal and gain control holds in a multibranch framework, we extended the experiment in Figure 2J by co-activating two or more dendritic clusters on different branches with a distributed background (Figures 3A–3C). While two co-activated clusters with NMDAR spikes increased the burst propensity (∼10 repetitive trials), indicating that multibranch NMDAR spikes cooperatively enhance somatic gain, gradually increasing the number of clusters any further did not result in an appreciable difference (Figure 3D). Further, the regulation of burst generation by the dynamics of the NMDA plateau, characterized by the AUC, as previously shown in Figures 2L and 2M, still holds under a multibranch framework (Figure 3E).

We then set out to corroborate the role of characteristic dendritic nonlinearities (i.e., Na^+ d-spikes vs. NMDA d-spikes) under multicluster co-activation. We chose ten clusters across various branches and co-activated them in groups of four (Figure 3F). When at least one cluster with a Na^+ d-spike was evoked (marked in red), the temporal precision of somatic output was improved (Figure 3G). This suggests that Na^+ d-spikes regulate the temporal precision in a "winner-takes-all" manner, whereby precision is guaranteed as long as at least one Na^+ d-spike is present (Figure 3H). Additional dendritic Na^+ spikes from other dendritic branches improve the temporal precision slightly but not significantly (Figure S7A). Interestingly, additional NMDAR spikes without a Na^+ spikelet also slightly improved the temporal precision (5.5 ± 4.5 ms with four NMDAR d-spikes), possibly due to the enhancement in axo-somatic responsivity, but not to the extent when at least one Na^+ d-spike was present (2.1 ± 2.1 ms with four clusters, at least one of which shows a Na^+ spikelet) (Figure S7B).

Cluster-evoked precision and gain under noisy *in vivo*-like states

Under awake *in vivo* conditions, neurons are constantly bombarded by synaptic inputs and are in high conductance. How

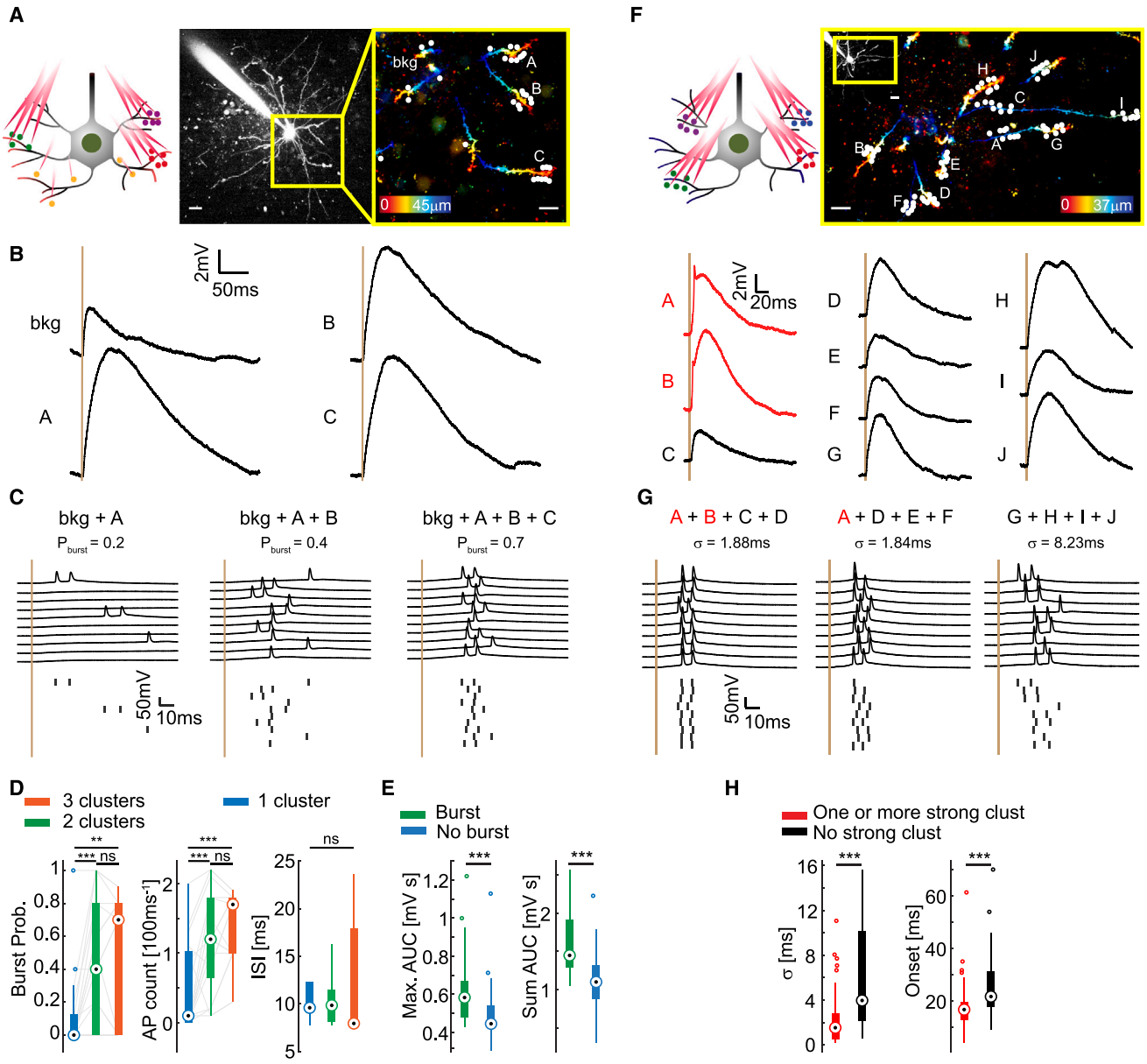

Figure 3. Multibranch control of somatic AP dynamics

(A) Schematic of three dendritic clusters (A, B, C) from different branches paired with the distributed background synapses (bkg). Scale bars, 20 μm (main) and 10 μm (inset).

(B) Uncaging-evoked waveform of each cluster and background synapses.

(C) Somatic burst propensity (ten repetitive trials) evoked by gradually increasing the number of co-activated clusters along with background synapses.

(D) Co-activation of multibranch dendritic clusters increases the burst probability (Mann-Whitney-Wilcoxon test, $n = 17$ groups of clusters from 13 cells, $^{**}p < 0.01$, $^{***}p < 0.005$).

(E) Both the maximum area under the curve (Max AUC) and the cumulative sum of the AUC across all co-activated clusters (Sum AUC) correlate with somatic burst generation (Mann-Whitney-Wilcoxon test, $n = 23$ multibranch uncaging patterns evoking bursts and 29 evoking single APs from 25 cells, $p < 0.005$).

(F) Schematic depicting four clusters co-activated across the basal dendritic arbor. Scale bars, 20 μm (main) and 10 μm (inset). Bottom: d-spikes evoked by holographic uncaging of each cluster.

(G) Four clusters are co-activated in different combinations.

(H) Under the multibranch framework, the presence of at least one strong cluster improves the precision and onset time of somatic APs (Mann-Whitney-Wilcoxon test, $n = 34$ multibranch uncaging patterns with at least one strong cluster and 27 with only weak clusters from 25 cells, $p < 0.005$).

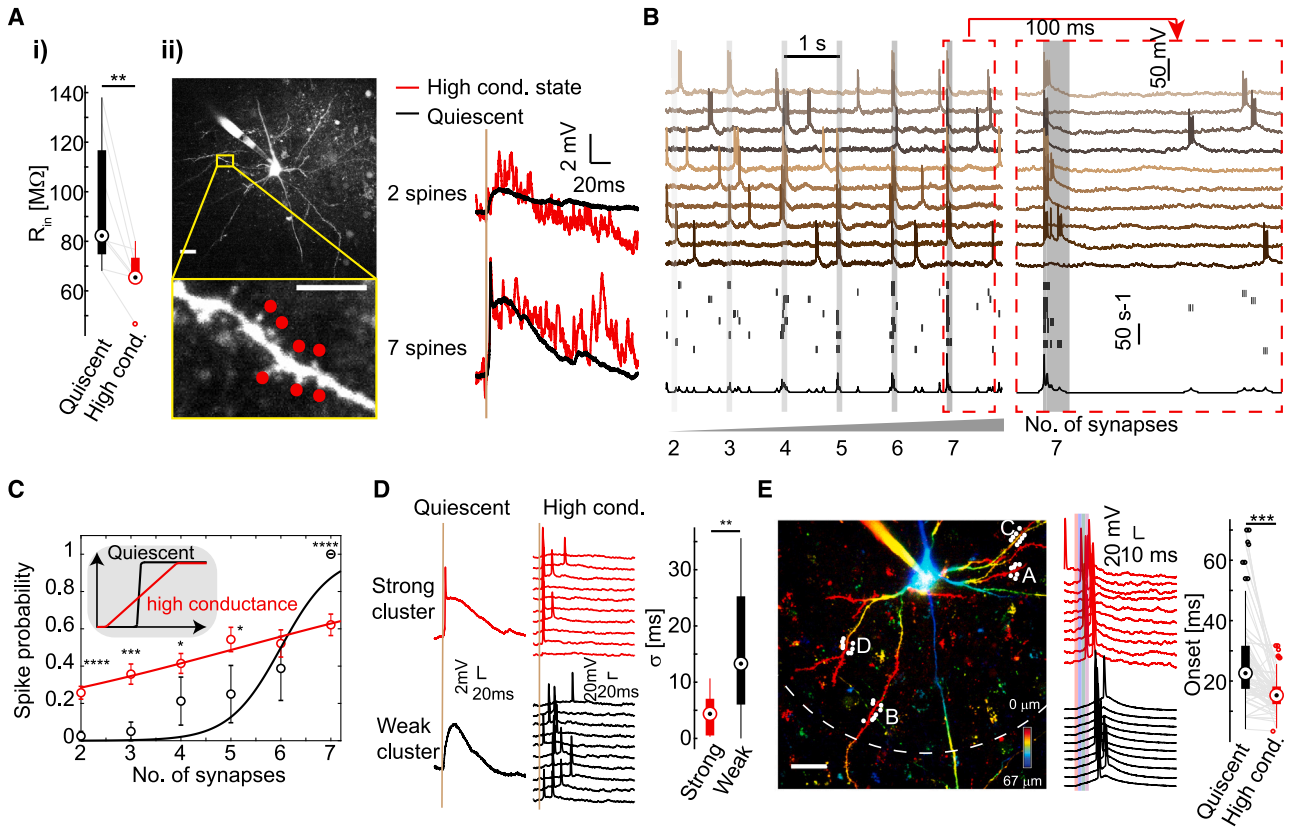

(legend on next page)

do synaptic inputs, including clusters, integrate under such high conductance and noisy background conditions?

Under the *in vivo*-like condition, two aspects will most likely impact the efficiency of dendritic nonlinearities: (1) the background conductance will decrease the resistance of the neuron and impact integration across dendritic branches; and (2) back-propagating AP resets could inactivate voltage-gated ion channels in the dendritic branches, thus impacting dendritic nonlinearities. To test this, we mimicked the high-conductance condition, characterized by low input resistance, noisy membrane fluctuations, a highly depolarized RMP, and a significant amount of background AP firing, via a dynamic clamp at the cell body (see STAR Methods) and assayed its impact on multiplexed synaptic integration (Figure 4) To ensure our results reflected spike output dynamics encountered *in vivo*, we matched our results to electrophysiological recordings from L5 of the awake mouse barrel cortex (S1) under feedforward sensory sweeps (whisker touch). Our results revealed time-locked single APs and bursts in response to the sensory stimuli (Figures S8A–S8F) superimposed on an ongoing background firing of 2–6 Hz (Figure S8G).

The high-conductance dynamic clamp significantly decreases the input resistance (R_{in} = 67 ± 10 MΩ) compared to the quiescent state (R_{in} = 94 ± 27 MΩ) (Figure 4Ai), consistent with the range obtained from whole-cell recordings from L5 neurons in the awake S1.[60] Noisy membrane fluctuations (2.46 ± 0.53 mV) resembling *in vivo* recordings[61] and increased background firing rates (4.72 ± 3.61 Hz) (Figure S9A) matched our *in vivo* recordings (Figure S8), in line with recent reports.[62] We performed holographic uncaging across a cluster of synapses under this high-conductance state (Figure 4Aii). Strikingly, the characteristic cluster-uncaging-evoked dendritic Na^+ spikelet feature was preserved under the high-conductance state.

To justify our conductance clamp, the conductance visibility observed from the soma approximates to ∼120 μm from the soma for L5 PNs[25,63] (Figure S9B and STAR Methods). Moreover, given cable-like properties and the mismatch in input resistances between the soma and basal dendrites, synaptic conductance generated across basal arbors is also expected to be visible at the soma. Therefore, a dynamic conductance injected at the soma robustly reflects widespread basal dendritic drive.[25,63] Given that dendritic conductance visibility spans ∼100 μm, it is a reasonable approximation for elucidating the effect of high conductance on synaptic integration.

We started with varying the number of co-activated spines in a cluster to study the integration of clustered synapses in the high-conductance state. Despite the background noise and ongoing voltage resets, spike time and rate modulation can be observed when around 6–7 clustered spines are co-activated (Figure 4B). Notably, in some trials, co-activation of only two or three synapses within the cluster would result in a somatic spike, unmasking an effect whereby a weak synaptic drive that was usually insufficient to modulate the somatic output under quiescent conditions now had a finite probability to generate a somatic AP under the high-conductance state (Figure 4C). Significantly, this result shows an improved dynamic range at the level of individual synapses, enabling probabilistic gating of AP output under a high-conductance state. This result builds on previous computational predictions,[38,39] providing a foundational demonstration of synaptic resolution efficacy on spike generation under noisy backgrounds. This result also sets up an important test: does the high-conductance state quench the formation of dendritic nonlinearities, thereby linearizing the spike probability as a function of increasing input intensity (number of synapses)? We probed the Na^+ d-spike-related somatic precision under the high-conductance state to test whether this was the case. We observed that the clusters evoking a Na^+ d-spike under a quiescent state led to higher AP precision even under noisy backgrounds and high-conductance states (Figure 4D). This result supports the notion that dendritic nonlinearity-induced spike precision at the soma has not been quenched and dictates the temporal profile of somatic APs amid ongoing activity.

By holographically co-activating clusters from different branches under a high-conductance state and comparing the spiking response to the quiescent state (Figure 4E), we observed a faster spike onset and higher spike and burst probability (Figure S9C) that is potentially due to a combination of shorter time constant, stochastic excitability from the background fluctuation, and depolarization of V_m closer to the threshold. These indicate a faster and more efficient integration of multibranch

Figure 4. Multibranch spike timing and gain regulation under high background conductance conditions

(A) (i) Lower input resistance under high conductance (Wilcoxon signed-rank test, n = 8 cells, $p < 0.01$). (ii) Holographic uncaging of clustered spines under high conductance. Scale bars, 20 μm (main) and 5 μm (inset).

(B) Temporal firing rate (bottom, black) evoked by co-activation of increasing spines in a cluster under high conductance.

(C) Spike probability as a function of co-activated synapses under quiescent and high-conductance states (Mann-Whitney-Wilcoxon test, n = 14 clusters from 8 neurons, $^*p < 0.05$, $^{**}p < 0.01$, $^{***}p < 0.005$, $^{****}p < 0.001$). Inset: theoretically expected trend.

(D) Na^+ d-spike-mediated spike precision is maintained under high-conductance conditions (Mann-Whitney-Wilcoxon test, n = 13 strong and 37 weak clusters from 25 cells, $p < 0.01$).

(E) Somatic spikes evoked by holographic uncaging of four clusters (inter-cluster stimulation interval 3 ms) show higher temporal resolution under high conductance (red) than quiescence (black) (Wilcoxon signed-rank test, n = 82 holographic uncaging patterns from 21 neurons, $p < 0.001$). Scale bar, 20 μm.

(F) Holographic uncaging of clustered and distributed synapses under high conductance. Scale bars, 20 μm (main) and 10 μm (inset).

(G) The quiescent-state holographic uncaging response of each cluster (A, B, C) and the background synapses (bkg) in (F). Cluster A evokes a Na^+ d-spike (red).

(H) Somatic spikes evoked by co-activating A, B, C, and the background synapses under quiescent state (top) and high-conductance state (bottom).

(I) Presence of at least one Na^+ d-spike dictates the temporal precision and onset delay under high-conductance states (Mann-Whitney-Wilcoxon test, n = 31 uncaging patterns with at least one strong cluster and 35 with only weak clusters from 26 cells, $p < 0.01$).

(J) Both the cumulative sum of AUC (left) and the maximum AUC (right) correlate with somatic burst generation under high-conductance states (Mann-Whitney-Wilcoxon test, n = 21 multibranch uncaging patterns evoking bursts and 28 evoking single APs from 26 neurons, $^*p < 0.05$, $^{**}p < 0.01$).

(K) Co-activation of increasing numbers of dendritic clusters increases the burst probability, AP counts, and interspike interval (ISI) (Mann-Whitney-Wilcoxon test, n = 27 uncaging patterns with 1 cluster, 22 with 2 clusters, 12 with 3 clusters from 13 neurons, $^*p < 0.05$, $^{**}p < 0.01$).

information. However, the AP jitter created by the same synaptic input patterns (Na^+ d-spikes and NMDA spikes) did not significantly differ between the low- and high-conductance states (Figure S9D).

We performed multibranch holographic uncaging experiments, as in Figure 3, but under high-conductance states (Figures 4F and 4G). Similarly, we observed the ''winner-takes-all'' regulation of somatic output by Na^+ d-spikes (Figure 4H), whereby a single Na^+ d-spike regulates overall precision (Figure 4I). While the burst probability is generally higher under the high-conductance state, the correlation between large NMDAR plateau and higher burst propensity is preserved (Figure 4J). More spikes are added by co-activating an increasing number of NMDAR d-spikes (Figure 4K), suggesting that dendritic nonlinearities do not saturate the output gain under the high-conductance state. Although the subsequent spikes appear jittered (jitter of the first spike 9.4 ± 8.6 ms, jitter of the second spike 12.0 ± 10.0 ms, n = 22 holographic patterns), they improve responsivity and provide a more dynamic temporal structure to the somatic output, potentially benefiting the multiplexing across multiple branches *in vivo*.

Multibranch information is multiplexed and barcoded through spike temporal structures

If two different clusters evoke Na^+ d-spikes, or both evoke NMDAR plateaus without a Na^+ component, would they elicit a distinguishable spiking output? To answer this question, we need a metric that encodes synaptic streams within the structure of somatic AP trains. Thus, to reveal temporal signatures embedded in the spike train structure and considering the stochastic nature of somatic spike generation, we used principal component regression (PCR) to evaluate the similarity/separability of spike temporal structures.[64]

We defined two different spatial-temporal uncaging patterns, for example, sequential uncaging on clusters A, B, C, and D as pattern 1 and B, A, C, and D as pattern 2 (Figure 5Ai). Each pattern was stimulated at no more than 1 Hz for ten trials to prevent any form of synaptic potentiation[65] (Figure 5AI, right)). We extracted and aligned a 100-ms window after uncaging onset (Figure 5Aii) before extracting the spike time (Figure 5Aiii). We then convolved the binary spike train with an EPSP-shape double exponential kernel to generate uncaging-evoked spike traces weighted by the time after spiking (Figure 5Aiv). We computed the correlation coefficient matrix over these 20 spike trains (Figure 5B), which revealed distinct intrinsic spike structures underlying each uncaging pattern despite the stochastic background and spike-generation variability. We performed a PCR using the pattern-evoked spike train structures (Figure 5C, see STAR Methods). After projecting the kernel-filtered spike trains to the principal component space (Figure S10A, see STAR Methods), we performed linear regression to segregate spike trains evoked with different uncaging patterns (Figure 5D). We found that the linear regression R^2 (0.51 ± 0.23) between different uncaging patterns is higher than the shuffled baseline (0.33 ± 0.11), and the application of AP5 decreases the R^2 value to the baseline level (Figure 5E). This linear separability is robust under various E/I (excitatory/inhibitory conductance) ratios (Figure 5F), suggesting that basal dendritic nonlinearities enable linear separation of spatial-temporal presynaptic input patterns, including under the presence of back-propagating voltage resets (Figures 5G and 5H). We corroborate this method by examining the separation between uncaging-evoked responses and spontaneous spikes (Figures S10B–S10D). The multicluster uncaging-evoked spikes are separable from the background created by the dynamic clamp, and AP5 abolishes this separability. Importantly, two randomly sampled groups of spontaneous spike trains are not separable given this approach, justifying the PCR approach. Taken together, we show that the PCR R^2 value can serve as a metric to quantify the multiplexing of multiple synaptic inputs.

Dendritic Na^+ spikes enhance the efficiency of sequence discrimination

Since Na^+ d-spikes enhance temporal precision, we investigated to what extent Na^+ d-spikes promote the classification of presynaptic patterns, since they tighten the trial-to-trial variability. In an L5 PN, we chose clusters evoking Na^+ d-spikes with different waveforms (A, B, C, denoted as strong cluster, marked in red) and another cluster evoking d-spike without a Na^+ spikelet (D, denoted as weak cluster, marked in black) (Figure 6A). Each cluster is co-activated with distributed synapses (bkg) under noisy conductance injection, and the temporal structures of APs evoked by each cluster are pairwise classified with PCR (Figures 6B and 6C). Note that the strong clusters (A, B, C) can be distinguished against the weak cluster (D) (R^2 = 0.29 ± 0.13). Importantly, A, B, and C can also be distinguished from each other (R^2 = 0.39 ± 0.07), suggesting that the Na^+ d-spike waveform shape is critical for classification. Consistent across multiple neurons, the classification between clusters with different Na^+ d-spikes (red) and clusters with and without Na^+ spikelet (blue) is above baseline (gray) (Figure 6D). This suggests that the Na^+ d-spikes and their waveforms may be critical for generating stable spike patterns that benefit classification and segmentation.

While Na^+ d-spike regulates the precise timing of somatic AP, we characterized whether it enables the discrimination of different input sequences. As an example, we chose five clusters (A, B, C, D, E), with one showing a Na^+ d-spike feature (denoted as A, Figure 6E). We paired the clusters into two groups, ABCD (Figure 6F, top), wherein one cluster (A) evoked a Na^+ d-spike, and EBCD (Figure 6F, bottom), wherein all clusters revealed a lack of a Na^+ d-spike. By shuffling the activation time of A and E within these two groups respectively, we observed that the activation time of A (strong cluster) changes the temporal profile of spikes by shifting the onset time of the precise spikes (median onset delay 3.8 ms, 6.6 ms, 8.2 ms, and 9.5 ms when A is the 1st, 2nd, 3rd, and 4th activated cluster, respectively), while changing the activation time of E (weak cluster) does not alter the spike temporal structure (median onset delay 13.3 ms, 7.4 ms, 10.8 ms, and 10.8 ms, respectively) (Figure 6G). The R^2 value is higher across different activation orders of ABCD (0.44 ± 0.26) compared to EBCD (0.26 ± 0.13) (Figure 6H, yellow dashed-line squares). We compared the separability of uncaging patterns with different activation sequences. Different sequences generated by shuffling the activation time of a Na^+ d-spike were separated (Figure 6I, red, 0.35 ± 0.22), but shuffling the activation time of an NMDAR d-spike resulted in poor

CellPress
OPEN ACCESS

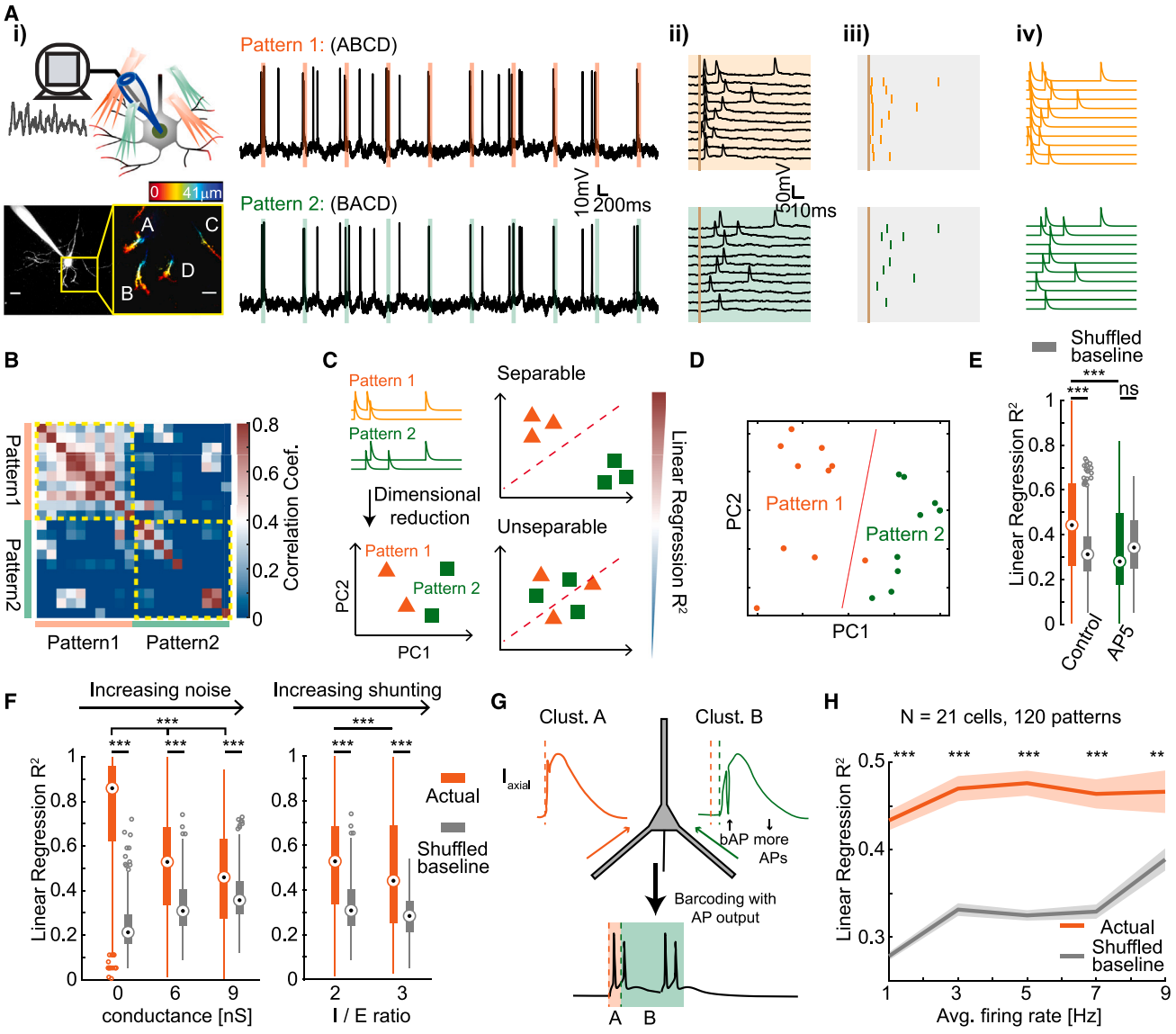

Figure 5. Dendritic nonlinearities enable barcoding of different spatial-temporal synaptic input patterns under *in vivo*-like conditions

(A) (i) Schematic and experimental output in which multiple dendritic clusters are sequentially activated (interval 3 ms). Scale bars, 20 μm (main) and 10 μm (inset). (ii) Uncaging-evoked somatic responses in the 100-ms window after the onset of the first uncaging event (shaded line). (iii) The uncaging-evoked spike raster. (iv) The binary spikes convolved with an EPSP-shape kernel.

(B) Correlation coefficient matrix of (Aiv).

(C) Principal component regression (PCR) schematic between two uncaging patterns.

(D) Linear segregation of uncaging-evoked responses in (A).

(E) Pairwise PCR R^2 values between two uncaging patterns are higher than the shuffled baseline under control but not under AP5 (Mann-Whitney-Wilcoxon test between control and ap5, Wilcoxon signed-rank test between R^2 and baseline (gray), n = 120 uncaging patterns, 1,477 pairs of pattern classification from 21 neurons for controls, and 17 uncaging patterns, 96 pairs of pattern classification from 5 neurons with AP5, $p < 0.0001$).

(F) The separability is robust under varying amounts of background conductance (n = 423 pairs of pattern classification from 21 neurons, Mann-Whitney-Wilcoxon test between different conductance or inhibitory drive, Wilcoxon signed-rank test between R^2 and baseline (gray), $p < 0.0001$).

(G) A possible barcoding mechanism under ongoing background firing.

(H) The separability between uncaging patterns (orange) as a function of background firing rate in comparison to the baseline (gray) (n = 525, 279, 283, 159, 57 pairs of pattern classification [from left to right] from 21 neurons, Wilcoxon signed-rank test, $^{**}p < 0.01$, $^{***}p < 0.0001$).

separability and classification (blue, 0.26 ± 0.18) Our results reveal that basal dendrites multiplex various synaptic input streams across branches, which can be classified based on spike structures evoked by distinct dendritic nonlinearities. Notably, the presence of Na^+ d-spikes helps structure the somatic spike train, while NMDA plateau potentials aid in gain

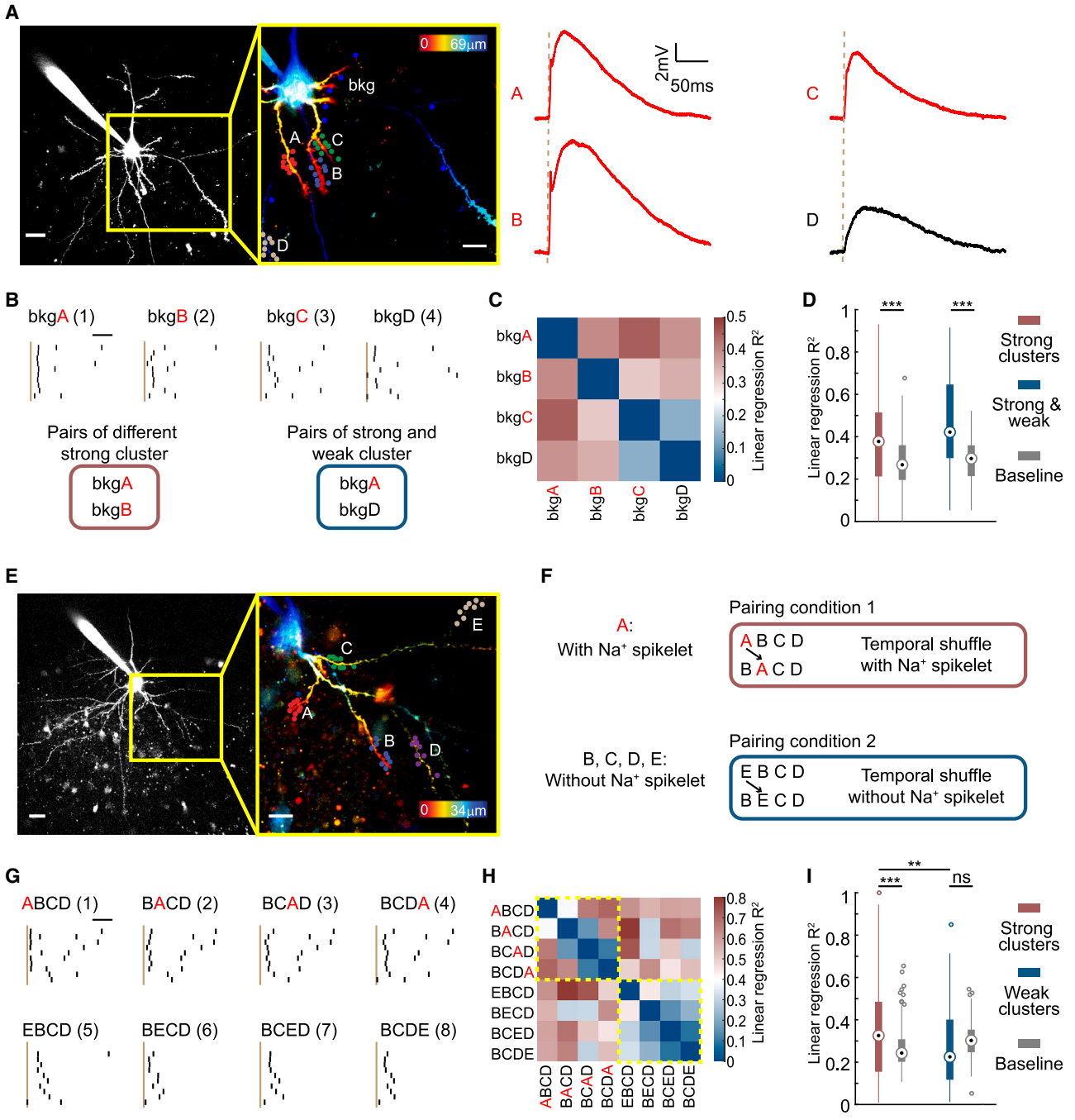

Figure 6. Classification between different spatial-temporal synaptic input patterns is enhanced by Na^+ d-spikes

(A) Holographic uncaging response of four clusters across the basal dendrites, among which clusters A, B, and C evoke Na^+ d-spikes (strong clusters, red), and cluster D evokes a d-spike without a Na^+ component (weak cluster, black). Scale bars, 20 μm (main) and 10 μm (inset).

(B) (Top) Somatic spike evoked by each cluster co-activated with the distributed synapses under background noisy conductance. (Bottom) Example of classification between a pair of strong clusters (red) and classification between a strong and a weak cluster (blue).

(C) Pairwise R^2 values across the four clusters in (B).

(D) The separability between two strong clusters (red) or between one strong and one weak cluster (blue) compared to the baseline (gray) ($n = 225$ pairs of strong clusters, 69 pairs of strong and weak clusters from 21 cells, Wilcoxon signed-rank test, $p < 0.0001$).

(E) Similar to (A), but with five different clusters; only A evokes Na^+ d-spikes (red).

(F) Classification is performed for two pairing conditions of uncaging patterns, one with a temporal shuffle of a strong cluster (red) and the other with a temporal shuffle of a weak cluster (blue).

(legend continued on next page)

control. Strikingly, the order of Na^+ spikes among different patterns matters and so does the duration of the NMDA spike. Critically, such barcoding of the somatic spike structure is maintained even under high-conductance states, including in the presence of back-propagating voltage resets.

DISCUSSION

We customized, characterized, and performed a 3D two-photon SLM-based holographic transmitter uncaging across multiple basal dendritic arbors of L5 PNs under quiescent and *in vivo*-like conditions. We combined holographic uncaging with whole-cell electrophysiology, dynamic clamp, and biophysical modeling. We examined how co-active dendritic nonlinearities across multiple branches multiplex at the soma to control somatic spike timing and gain. Finally, we explored the role of synaptic clusters in enabling temporal precision and gain under *in vivo*-like conditions and how this unique regulation enables the separation and classification of different spatial-temporal synaptic input patterns based on somatic spike structures.

Basal dendrites exhibit a rich repertoire of regenerative dendritic spikes, and these events are a strong function of synchronous synaptic inputs. There is mounting evidence that such synapses are clustered across a 5- to 10-μm length scale.[22,28,66] Most of our understanding of clustered synaptic stimulation, however, has come from uncaging-evoked responses across these short dendritic segments using rapidly switching galvanometric mirrors.[16] The ability to stimulate clusters of synapses across the entire dendrite and multiple dendrites opens up the possibility of querying synaptic and dendritic integration, cooperativity, and spike-generation mechanisms in much greater detail.

Clustered synapses have been envisaged to underlie feature binding,[67] memory storage,[68,69] and pattern recognition.[44] This would imply that clustered synapses should be able to modulate the firing properties of the neuron meaningfully, for example via dynamic changes in threshold.[70] Signaling such synchronized inputs in the presence of voltage-gated channels, ongoing background activity, and noise—in the form of both stochastic membrane potential fluctuations and a background rate code—is critical for efficient neural computation.[71] We investigated the mechanisms through which such clustered activation across single and multiple dendritic segments impacts AP generation. Our findings, in agreement with previous reports,[18] (Figure 2) demonstrate that nonlinear Na^+-mediated dendritic spikes drive AP activity with high precision, while NMDAR plateau potentials mediate gain control. Importantly, dendritic Na^+ spikes ensure temporal precision by eliciting the sharp voltage fluctuation that recruits the stochastic gating effect of somatic voltage-gated ion channels. Since dendritic Na^+ spikes have been observed to occur at high rates *in vivo*,[72] this could imply that stochastic gating is critical for energy-efficient computations.[57,58] Our study substantially adds to the growing understanding of dendritic integration when considering a multibranch framework with multiple dendritic nonlinearities co-activated. We find that Na^+ dendritic spikes barcode the somatic output while NMDAR d-spikes modulate somatic gain, and together they help structure the spike train over critical time windows (Figure 3). Importantly, the cooperative and active integration properties in the dendrites support the idea that temporal barcoding of the somatic structure through NMDA and Na^+ d-spikes could serve as a powerful mechanism to bind different inputs over a window of time, especially since such nonlinearities depend on recent and ongoing activity in the local network. Furthermore, localized dendritic inhibition across basal dendritic arbors suggests that L5 PNs can integrate and multiplex diverse feedforward streams over a broad and tunable conductance range.[60,73]

Neurons *in vivo* are characterized by noisy membrane fluctuations, low input resistance, and depolarized RMPs. We examined how clustered synaptic inputs, which result in dendritic nonlinearities under quiescent conditions, impact AP generation under *in vivo*-like conditions. Computational efforts examining integration under such conditions have revealed two key principles[38]: gain modulation via conductance noise and increased temporal resolution. Our results show enhanced somatic AP response and amplification of weak inputs (2–3 co-activated spines that normally fail to elicit somatic spikes under a quiescent state) (Figure 4C). This result suggests that sparse inputs and their interaction with a noisy background might be capable of probabilistically modulating somatic spiking, especially *in vivo*, which aligns with previous theoretical predictions.[38,74] Clustered synaptic inputs, in contrast, could still lead to dendritic nonlinearities despite the reduced input resistance and constantly invading back-propagated APs[75] and profoundly impacted AP generation via precision and gain (Figures 4D–4K). This suggests that somatic APs, compared to NMDAR-mediated nonlinearities under conditions of high conductance, equilibrate rapidly in the dendrite and cause minimal voltage resets.[9] This ability of clustered synaptic input to maintain efficient somatic control amid ongoing noise[66] could endow PNs with the ability to perform precision and rate coding strategies in parallel.[2,38]

The basal dendritic arborization shows high heterogeneity in morphology, ion channel distribution, and presynaptic terminal arrangement.[21,37,76] With strengthened temporal resolution and equalization under the high-conductance condition, the spatial-temporal arrangement of the presynaptic inputs should be reflected in the somatic output in terms of time and rate of APs. Our results show that different spatial-temporal synaptic inputs integrate to generate distinguishable somatic spike structures (Figures 5 and 6). Importantly, dendritic Na^+ spikes promote the classification, suggesting that precise timing plays a critical role in dendritic multiplexing. A recent computational study suggests that this embedded computational power in dendritic heterogeneity can be harvested and strengthened with

(G) Somatic spikes evoked by eight different uncaging patterns as shown in (F).
(H) The pairwise R^2 values are high in the ABCD quadrant but low in the EBCD quadrant (yellow boxes).
(I) R^2 values between different uncaging sequences with (red) and without (blue) a strong cluster compared to the baseline (gray) (Mann-Whitney-Wilcoxon test between different pairing conditions, Wilcoxon signed-rank test between R^2 and baseline, n = 177 pairs of temporal shuffling strong clusters, 128 pairs of temporal shuffling weak clusters from 21 cells, $^{**}p < 0.005$, $^{***}p < 0.001$).

synaptic plasticity.[77] Together, this could enable the *in vivo* neuron to detect, selectively strengthen, and bind certain presynaptic input patterns despite the variability of spike generation. In conclusion, basal dendritic nonlinearities serve as a putative substrate for simultaneous computations at different sites, which can be bound together over a window of time reflected in a structured somatic spike train, enabling downstream targets to classify the synaptic combinations involved.

Overall, we reveal a model in which multibranch synaptic input patterns can be multiplexed via barcoding of somatic spike structure. The proposed mechanisms could help explain how neurons in the awake brain perform feature binding[67,78] despite ongoing background activity.

Limitations of the study

In this study, we did not take into account the impact of the location of synapses and their cooperation within a single branch.[79] Under high-conductance conditions, this cooperativity may be even more exaggerated owing to an equalization of impedance across the arbor.[38] Moreover, the cooperation within a single branch and across branches can further influence the processing of incoming signals by dynamically adjusting the level of local signal amplification, which could in turn affect the firing pattern of the cell and its information encoding. Another limitation is the amount of power available at the sample plane at uncaging relevant wavelengths (740 nm), which directly affects the number of spines that can be simultaneously targeted.

STAR★METHODS

Detailed methods are provided in the online version of this paper and include the following:

- KEY RESOURCES TABLE
- RESOURCE AVAILABILITY
  - Lead contact
  - Materials availability
  - Data and code availability
- EXPERIMENTAL MODEL AND STUDY PARTICIPANT DETAILS
  - Animals
- METHOD DETAILS
  - Acute slice preparation
  - Electrophysiological recording
  - Dynamic clamp
  - Simultaneous two photon imaging and 3D holographic glutamate uncaging
  - PSF estimation of holographic uncaging spots
  - Pharmacology
  - Principal component regression of spike temporal structure
  - Surgery procedures
  - Virus injection
  - Intrinsic optical imaging
  - *In vivo* silicon probe recordings
  - Point-source stochastic Hodgkin-Huxley model
  - Analytical estimation of conductance visibility in the dendrites
  - L5 PN sub-type classification
- QUANTIFICATION AND STATISTICAL ANALYSIS

SUPPLEMENTAL INFORMATION

Supplemental information can be found online at https://doi.org/10.1016/j.celrep.2024.114413.

ACKNOWLEDGMENTS

We thank all members of the NanoNeurotechnology lab for critical feedback. This project was partly supported by R21 EB029740 (NIH Trailblazer), HFSP RGY0069, Ralph E. Powe Junior Faculty Enhancement Award to K.J., and the Purdue Institute for Integrative Neuroscience. This work is also based upon efforts supported by EMBRIO Institute, contract #2120200, a National Science Foundation Biology Integration Institute. This effort was sponsored in whole or in part by the Central Intelligence Agency (CIA), through CIA Federal Labs. The US Government is authorized to reproduce and distribute reprints for Governmental purposes notwithstanding any copyright notation thereon. The views and conclusions contained herein are those of the authors and should not be interpreted as necessarily representing the official policies or endorsements, either expressed or implied, of the Central Intelligence Agency.

AUTHOR CONTRIBUTIONS

S.X., S.Y., and K.J. designed experiments. S.X. performed *in vitro* and *in vivo* experiments, characterized the SLM microscope, analyzed the data, and made figures. S.Y. optimized and characterized the SLM microscope and assisted with uncaging experiments and analysis. S.X. and S.Y. wrote the original draft. K.J. conceived and supervised the overall study and wrote the final manuscript.

DECLARATION OF INTERESTS

The authors declare no competing interests.

Received: September 29, 2022
Revised: May 6, 2024
Accepted: June 12, 2024
Published: June 27, 2024

REFERENCES

1. London, M., Roth, A., Beeren, L., Häusser, M., and Latham, P.E. (2010). Sensitivity to perturbations in vivo implies high noise and suggests rate coding in cortex. Nature *466*, 123–127.
2. Tiesinga, P., Fellous, J.-M., and Sejnowski, T.J. (2008). Regulation of spike timing in visual cortical circuits. Nat. Rev. Neurosci. *9*, 97–107.
3. Duguid, I., and Sjöström, P.J. (2006). Novel presynaptic mechanisms for coincidence detection in synaptic plasticity. Curr. Opin. Neurobiol. *16*, 312–322.
4. Kampa, B.M., Letzkus, J.J., and Stuart, G.J. (2007). Dendritic mechanisms controlling spike-timing-dependent synaptic plasticity. Trends Neurosci. *30*, 456–463.
5. Pérez-Garci, E., Gassmann, M., Bettler, B., and Larkum, M.E. (2006). The GABAB1b isoform mediates long-lasting inhibition of dendritic Ca2+ spikes in layer 5 somatosensory pyramidal neurons. Neuron *50*, 603–616.
6. Larkum, M.E., Zhu, J.J., and Sakmann, B. (1999). A new cellular mechanism for coupling inputs arriving at different cortical layers. Nature *398*, 338–341.
7. Kampa, B.M., and Stuart, G.J. (2006). Calcium spikes in basal dendrites of layer 5 pyramidal neurons during action potential bursts. J. Neurosci. *26*, 7424–7432.
8. Takahashi, N., Ebner, C., Sigl-Glöckner, J., Moberg, S., Nierwetberg, S., and Larkum, M.E. (2020). Active dendritic currents gate descending cortical outputs in perception. Nat. Neurosci. *23*, 1277–1285.
9. Behabadi, B.F., and Mel, B.W. (2014). Mechanisms underlying subunit independence in pyramidal neuron dendrites. Proc. Natl. Acad. Sci. USA *111*, 498–503.
10. Tran-Van-Minh, A., Cazé, R.D., Abrahamsson, T., Cathala, L., Gutkin, B.S., and DiGregorio, D.A. (2015). Contribution of sublinear and supralinear dendritic integration to neuronal computations. Front. Cell. Neurosci. *9*, 67.

11. Kampa, B.M., Clements, J., Jonas, P., and Stuart, G.J. (2004). Kinetics of Mg2+ unblock of NMDA receptors: implications for spike-timing dependent synaptic plasticity. J. Physiol. *556*, 337–345.

12. Jayant, K., Hirtz, J.J., Plante, I.J.-L., Tsai, D.M., De Boer, W.D.A.M., Semonche, A., Peterka, D.S., Owen, J.S., Sahin, O., Shepard, K.L., and Yuste, R. (2017). Targeted intracellular voltage recordings from dendritic spines using quantum-dot-coated nanopipettes. Nat. Nanotechnol. *12*, 335–342.

13. Harnett, M.T., Makara, J.K., Spruston, N., Kath, W.L., and Magee, J.C. (2012). Synaptic amplification by dendritic spines enhances input cooperativity. Nature *491*, 599–602.

14. Schiller, J., Major, G., Koester, H.J., and Schiller, Y. (2000). NMDA spikes in basal dendrites of cortical pyramidal neurons. Nature *404*, 285–289.

15. Branco, T., and Häusser, M. (2011). Synaptic integration gradients in single cortical pyramidal cell dendrites. Neuron *69*, 885–892.

16. Lafourcade, M., van der Goes, M.-S.H., Vardalaki, D., Brown, N.J., Voigts, J., Yun, D.H., Kim, M.E., Ku, T., and Harnett, M.T. (2022). Differential dendritic integration of long-range inputs in association cortex via subcellular changes in synaptic AMPA-to-NMDA receptor ratio. Neuron *110*, 1532–1546.e4.

17. Schiller, J., and Schiller, Y. (2001). NMDA receptor-mediated dendritic spikes and coincident signal amplification. Curr. Opin. Neurobiol. *11*, 343–348.

18. Ariav, G., Polsky, A., and Schiller, J. (2003). Submillisecond precision of the input-output transformation function mediated by fast sodium dendritic spikes in basal dendrites of CA1 pyramidal neurons. J. Neurosci. *23*, 7750–7758.

19. Golding, N.L., and Spruston, N. (1998). Dendritic sodium spikes are variable triggers of axonal action potentials in hippocampal CA1 pyramidal neurons. Neuron *21*, 1189–1200.

20. Losonczy, A., Makara, J.K., and Magee, J.C. (2008). Compartmentalized dendritic plasticity and input feature storage in neurons. Nature *452*, 436–441.

21. Petreanu, L., Mao, T., Sternson, S.M., and Svoboda, K. (2009). The subcellular organization of neocortical excitatory connections. Nature *457*, 1142–1145.

22. Gökçe, O., Bonhoeffer, T., and Scheuss, V. (2016). Clusters of synaptic inputs on dendrites of layer 5 pyramidal cells in mouse visual cortex. Elife *5*, e09222.

23. Sjöström, P.J., and Häusser, M. (2006). A cooperative switch determines the sign of synaptic plasticity in distal dendrites of neocortical pyramidal neurons. Neuron *51*, 227–238.

24. Markram, H. (1997). A network of tufted layer 5 pyramidal neurons. Cereb. Cortex *7*, 523–533. https://doi.org/10.1093/cercor/7.6.523.

25. Williams, S.R. (2004). Spatial compartmentalization and functional impact of conductance in pyramidal neurons. Nat. Neurosci. *7*, 961–967.

26. Dembrow, N.C., and Spain, W.J. (2022). Input rate encoding and gain control in dendrites of neocortical pyramidal neurons. Cell Rep. *38*, 110382.

27. Takahashi, N., Kitamura, K., Matsuo, N., Mayford, M., Kano, M., Matsuki, N., and Ikegaya, Y. (2012). Locally synchronized synaptic inputs. Science *335*, 353–356.

28. Scholl, B., Wilson, D.E., and Fitzpatrick, D. (2017). Local order within global disorder: synaptic architecture of visual space. Neuron *96*, 1127–1138.e4.

29. Jia, H., Rochefort, N.L., Chen, X., and Konnerth, A. (2010). Dendritic organization of sensory input to cortical neurons in vivo. Nature *464*, 1307–1312.

30. Larkum, M.E., and Nevian, T. (2008). Synaptic clustering by dendritic signalling mechanisms. Curr. Opin. Neurobiol. *18*, 321–331.

31. Poirazi, P., Brannon, T., and Mel, B.W. (2003). Pyramidal neuron as two-layer neural network. Neuron *37*, 989–999.

32. Jadi, M.P., Behabadi, B.F., Poleg-Polsky, A., Schiller, J., and Mel, B.W. (2014). An augmented two-layer model captures nonlinear analog spatial integration effects in pyramidal neuron dendrites. Proc. IEEE *102*, 1–798.

33. Major, G., Polsky, A., Denk, W., Schiller, J., and Tank, D.W. (2008). Spatiotemporally graded NMDA spike/plateau potentials in basal dendrites of neocortical pyramidal neurons. J. Neurophysiol. *99*, 2584–2601.

34. Polsky, A., Mel, B., and Schiller, J. (2009). Encoding and decoding bursts by NMDA spikes in basal dendrites of layer 5 pyramidal neurons. J. Neurosci. *29*, 11891–11903.

35. Hill, D.N., Varga, Z., Jia, H., Sakmann, B., and Konnerth, A. (2013). Multibranch activity in basal and tuft dendrites during firing of layer 5 cortical neurons in vivo. Proc. Natl. Acad. Sci. USA *110*, 13618–13623.

36. Remy, S., Csicsvari, J., and Beck, H. (2009). Activity-dependent control of neuronal output by local and global dendritic spike attenuation. Neuron *61*, 906–916.

37. Nevian, T., Larkum, M.E., Polsky, A., and Schiller, J. (2007). Properties of basal dendrites of layer 5 pyramidal neurons: a direct patch-clamp recording study. Nat. Neurosci. *10*, 206–214.

38. Destexhe, A., Rudolph, M., and Paré, D. (2003). The high-conductance state of neocortical neurons in vivo. Nat. Rev. Neurosci. *4*, 739–751.

39. Hô, N., and Destexhe, A. (2000). Synaptic background activity enhances the responsiveness of neocortical pyramidal neurons. J. Neurophysiol. *84*, 1488–1496.

40. Fernandez, F.R., Broicher, T., Truong, A., and White, J.A. (2011). Membrane voltage fluctuations reduce spike frequency adaptation and preserve output gain in CA1 pyramidal neurons in a high-conductance state. J. Neurosci. *31*, 3880–3893.

41. Mainen, Z.F., and Sejnowski, T.J. (1995). Reliability of spike timing in neocortical neurons. Science *268*, 1503–1506.

42. Shu, Y., Hasenstaub, A., Badoual, M., Bal, T., and McCormick, D.A. (2003). Barrages of synaptic activity control the gain and sensitivity of cortical neurons. J. Neurosci. *23*, 10388–10401.

43. Ujfalussy, B.B., Makara, J.K., Lengyel, M., and Branco, T. (2018). Global and multiplexed dendritic computations under in vivo-like conditions. Neuron *100*, 579–592.e5.

44. Bicknell, B.A., and Häusser, M. (2021). A synaptic learning rule for exploiting nonlinear dendritic computation. Neuron *109*, 4001–4017. e4010.

45. Kumar, A., Schiff, O., Barkai, E., Mel, B.W., Poleg-Polsky, A., and Schiller, J. (2018). NMDA spikes mediate amplification of inputs in the rat piriform cortex. Elife *7*, e38446.

46. Losavio, B.E., Iyer, V., and Saggau, P. (2009). Two-photon microscope for multisite microphotolysis of caged neurotransmitters in acute brain slices. J. Biomed. Opt. *14*, 064033.

47. Lutz, C., Otis, T.S., DeSars, V., Charpak, S., DiGregorio, D.A., and Emiliani, V. (2008). Holographic photolysis of caged neurotransmitters. Nat. Methods *5*, 821–827.

48. Yang, S., Emiliani, V., and Tang, C.-M. (2014). The kinetics of multibranch integration on the dendritic arbor of CA1 pyramidal neurons. Front. Cell. Neurosci. *8*, 127.

49. Nikolenko, V., Watson, B.O., Araya, R., Woodruff, A., Peterka, D.S., and Yuste, R. (2008). SLM Microscopy: Scanless Two-Photon Imaging and Photostimulation with Spatial Light Modulators. Front. Neural Circuits *2*, 5.

50. Go, M.A., Mueller, M., Castañares, M.L., Egger, V., and Daria, V.R. (2019). A compact holographic projector module for high-resolution 3D multi-site two-photon photostimulation. PLoS One *14*, e0210564.

51. Weber, J.P., Andrásfalvy, B.K., Polito, M., Magó, Á., Ujfalussy, B.B., and Makara, J.K. (2016). Location-dependent synaptic plasticity rules by dendritic spine cooperativity. Nat. Commun. *7*, 1–14.

52. Gasparini, S., Migliore, M., and Magee, J.C. (2004). On the initiation and propagation of dendritic spikes in CA1 pyramidal neurons. J. Neurosci. *24*, 11046–11056.

53. Ellis-Davies, G.C.R. (2018). Two-photon uncaging of glutamate. Front. Synaptic Neurosci. *10*, 48.
54. Matsuzaki, M., Ellis-Davies, G.C., Nemoto, T., Miyashita, Y., Iino, M., and Kasai, H. (2001). Dendritic spine geometry is critical for AMPA receptor expression in hippocampal CA1 pyramidal neurons. Nat. Neurosci. *4*, 1086–1092.
55. Harvey, C.D., and Svoboda, K. (2007). Locally dynamic synaptic learning rules in pyramidal neuron dendrites. Nature *450*, 1195–1200.
56. Smith, M.A., Ellis-Davies, G.C., and Magee, J.C. (2003). Mechanism of the distance-dependent scaling of Schaffer collateral synapses in rat CA1 pyramidal neurons. J. Physiol. *548*, 245–258.
57. White, J.A., Rubinstein, J.T., and Kay, A.R. (2000). Channel noise in neurons. Trends Neurosci. *23*, 131–137.
58. Schneidman, E., Freedman, B., and Segev, I. (1998). Ion channel stochasticity may be critical in determining the reliability and precision of spike timing. Neural Comput. *10*, 1679–1703.
59. Chow, C.C., and White, J.A. (1996). Spontaneous action potentials due to channel fluctuations. Biophys. J. *71*, 3013–3021.
60. Zhao, W.-J., Kremkow, J., and Poulet, J.F.A. (2016). Translaminar cortical membrane potential synchrony in behaving mice. Cell Rep. *15*, 2387–2399.
61. Jayant, K., Wenzel, M., Bando, Y., Hamm, J.P., Mandriota, N., Rabinowitz, J.H., Plante, I.J.L., Owen, J.S., Sahin, O., Shepard, K.L., and Yuste, R. (2019). Flexible nanopipettes for minimally invasive intracellular electrophysiology in vivo. Cell Rep. *26*, 266–278.e5.
62. de Kock, C.P.J., Pie, J., Pieneman, A.W., Mease, R.A., Bast, A., Guest, J.M., Oberlaender, M., Mansvelder, H.D., and Sakmann, B. (2021). High-frequency burst spiking in layer 5 thick-tufted pyramids of rat primary somatosensory cortex encodes exploratory touch. Commun. Biol. *4*, 709.
63. Koch, C., Douglas, R., and Wehmeier, U. (1990). Visibility of synaptically induced conductance changes: theory and simulations of anatomically characterized cortical pyramidal cells. J. Neurosci. *10*, 1728–1744.
64. Chapin, J.K., and Nicolelis, M.A. (1999). Principal component analysis of neuronal ensemble activity reveals multidimensional somatosensory representations. J. Neurosci. Methods *94*, 121–140.
65. Inglebert, Y., and Debanne, D. (2021). Calcium and spike timing-dependent plasticity. Front. Cell. Neurosci. *15*, 727336.
66. Scholl, B., Thomas, C.I., Ryan, M.A., Kamasawa, N., and Fitzpatrick, D. (2021). Cortical response selectivity derives from strength in numbers of synapses. Nature *590*, 111–114.
67. Costa, R.P., and Sjöström, P.J. (2011). One cell to rule them all, and in the dendrites bind them. Front. Synaptic Neurosci. *3*, 5.
68. Gambino, F., Pagès, S., Kehayas, V., Baptista, D., Tatti, R., Carleton, A., and Holtmaat, A. (2014). Sensory-evoked LTP driven by dendritic plateau potentials in vivo. Nature *515*, 116–119.
69. Kerlin, A., Mohar, B., Flickinger, D., MacLennan, B.J., Dean, M.B., Davis, C., Spruston, N., and Svoboda, K. (2019). Functional clustering of dendritic activity during decision-making. Elife *8*, e46966.
70. Azouz, R., and Gray, C.M. (2000). Dynamic spike threshold reveals a mechanism for synaptic coincidence detection in cortical neurons in vivo. Proc. Natl. Acad. Sci. USA *97*, 8110–8115.
71. Silver, R.A. (2010). Neuronal arithmetic. Nat. Rev. Neurosci. *11*, 474–489.
72. Destexhe, A., and Mehta, M. (2022). Properties and computational consequences of fast dendritic spikes during natural behavior. Neuroscience *489*, 251–261.
73. Bennett, C., Arroyo, S., and Hestrin, S. (2013). Subthreshold mechanisms underlying state-dependent modulation of visual responses. Neuron *80*, 350–357.
74. Goetz, L., Roth, A., and Häusser, M. (2021). Active dendrites enable strong but sparse inputs to determine orientation selectivity. Proc. Natl. Acad. Sci. USA *118*, e2017339118.
75. Antic, S.D. (2003). Action potentials in basal and oblique dendrites of rat neocortical pyramidal neurons. J. Physiol. *550*, 35–50.
76. Acker, C.D., and Antic, S.D. (2009). Quantitative assessment of the distributions of membrane conductances involved in action potential backpropagation along basal dendrites. J. Neurophysiol. *101*, 1524–1541.
77. Bicknell, B.A., and Häusser, M. (2021). A synaptic learning rule for exploiting nonlinear dendritic computation. Neuron *109*, 4001–4017.e4010. https://doi.org/10.1016/j.neuron.2021.09.044.
78. Legenstein, R., and Maass, W. (2011). Branch-specific plasticity enables self-organization of nonlinear computation in single neurons. J. Neurosci. *31*, 10787–10802.
79. Behabadi, B.F., Polsky, A., Jadi, M., Schiller, J., and Mel, B.W. (2012). Location-dependent excitatory synaptic interactions in pyramidal neuron dendrites. PLoS Comput. Biol. *8*, e1002599.
80. Klapoetke, N.C., Murata, Y., Kim, S.S., Pulver, S.R., Birdsey-Benson, A., Cho, Y.K., Morimoto, T.K., Chuong, A.S., Carpenter, E.J., Tian, Z., et al. (2014). Independent optical excitation of distinct neural populations. Nat. Methods *11*, 338–346.
81. Boyden, E.S., Zhang, F., Bamberg, E., Nagel, G., and Deisseroth, K. (2005). Millisecond-timescale, genetically targeted optical control of neural activity. Nat. Neurosci. *8*, 1263–1268.
82. Hines, M.L., and Carnevale, N.T. (1997). The NEURON simulation environment. Neural Comput. *9*, 1179–1209.
83. Schneider, C.A., Rasband, W.S., and Eliceiri, K.W. (2012). NIH Image to ImageJ: 25 years of image analysis. Nat. Methods *9*, 671–675.
84. Pachitariu, M., Steinmetz, N.A., Kadir, S.N., Carandini, M., and Harris, K.D. (2016). Fast and accurate spike sorting of high-channel count probes with KiloSort. In Advances in Neural Information Processing Systems 29 (NIPS 2016).
85. Mathis, A., Mamidanna, P., Cury, K.M., Abe, T., Murthy, V.N., Mathis, M.W., and Bethge, M. (2018). DeepLabCut: markerless pose estimation of user-defined body parts with deep learning. Nat. Neurosci. *21*, 1281–1289.
86. Ting, J.T., Daigle, T.L., Chen, Q., and Feng, G. (2014). Acute brain slice methods for adult and aging animals: application of targeted patch clamp analysis and optogenetics. In Patch-Clamp Methods and Protocols, M. Martina and S. Taverna, eds. (Springer), pp. 221–242.
87. Ting, J.T., Lee, B.R., Chong, P., Soler-Llavina, G., Cobbs, C., Koch, C., Zeng, H., and Lein, E. (2018). Preparation of acute brain slices using an optimized N-methyl-D-glucamine protective recovery method. JoVE, e53825. https://doi.org/10.3791/53825-v.
88. Desai, N.S., Gray, R., and Johnston, D. (2017). A dynamic clamp on every rig. eNeuro *4*. https://doi.org/10.1523/ENEURO.0250-17.2017.
89. Destexhe, A., Rudolph, M., Fellous, J.-M., and Sejnowski, T.J. (2001). Fluctuating synaptic conductances recreate in vivo-like activity in neocortical neurons. Neuroscience *107*, 13–24.
90. Tønnesen, J., Katona, G., Rózsa, B., and Nägerl, U.V. (2014). Spine neck plasticity regulates compartmentalization of synapses. Nat. Neurosci. *17*, 678–685.
91. Cole, R.W., Jinadasa, T., and Brown, C.M. (2011). Measuring and interpreting point spread functions to determine confocal microscope resolution and ensure quality control. Nat. Protoc. *6*, 1929–1941.

STAR★METHODS

KEY RESOURCES TABLE

REAGENT or RESOURCE	SOURCE	IDENTIFIER
Bacterial and virus strains		
pAAV-FLEX-tdTomato	Klapoetke et al.[80]	Addgene AAV1; 28306-AAV1
pAAV-EF1a-double floxed-hChR2(H134R)-EYFP-WPRE-HGHpA	Boyden et al.[81]	Addgene AAVrg; 20298-AAVrg
Chemicals, peptides, and recombinant proteins		
Tetrodotoxin	Tocris	1078; CAS: 4368-28-9
D-AP5	Tocris	0106; CAS: 79055-68-8
Alexa Fluor 594 Hydrazide	Invitrogen	A10438
Alexa Fluor 488 Hydrazide	Invitrogen	A10436
Fluo-4, Pentapotassium Salt, cell impermeant	Invitrogen	F14200
FluoSpheres Carboxylate-Modified Microspheres	Invitrogen	F8803
Sodium chloride	Sigma-Aldrich	S9888; CAS: 7647-14-5
Potassium chloride	Sigma-Aldrich	P9333; CAS: 7447-40-7
Sodium bicarbonate	Sigma-Aldrich	S5761; CAS: 144-55-8
Sodium phosphate monobasic	Sigma-Aldrich	S8282; CAS: 7558-80-7
HEPES	Sigma-Aldrich	H4034; CAS: 7365-45-9
D-(+)-Glucose	Sigma-Aldrich	G8270; CAS: 50-99-7
Sucrose	Sigma-Aldrich	S0389; CAS: 57-50-1
Calcium chloride	Sigma-Aldrich	C8106; CAS: 10035-04-8
Magnesium chloride hexahydrate	Sigma-Aldrich	M2670; CAS: 7791-18-6
Adenosine 5'-triphosphate magnesium salt	Sigma-Aldrich	A9187; CAS: 74804-12-9
Guanosine 5′-triphosphate tris salt	Sigma-Aldrich	G9002; CAS: 103192-46-7
Phosphocreatine disodium salt hydrate	Sigma-Aldrich	P7936; CAS: 19333-65-4
Potassium gluconate	Sigma-Aldrich	P1847; CAS: 299-27-4
N-Acetyl-L-cysteine	Sigma-Aldrich	A7250; CAS: 616-91-1
N-Methyl-D-glucamine	Sigma-Aldrich	66930; CAS: 6284-40-8
Sodium hydroxide	Sigma-Aldrich	S8045; CAS: 1310-73-2
Potassium hydroxide	Sigma-Aldrich	221473; CAS: 1310-58-3
(+)-Sodium L-ascorbate	Sigma-Aldrich	A4034; CAS: 134-03-2
Sodium pyruvate	Sigma-Aldrich	P5280; CAS: 113-24-6
Thiourea	Sigma-Aldrich	T8656; CAS: 62-56-6
Hydrochloric acid	Sigma-Aldrich	320331; CAS: 7647-01-0
Deposited data		
Primary data	This paper	[Database] : [https://doi.org/10.5281/zenodo.11303995]
Experimental models: Organisms/strains		
Mouse: C57BL/6J	The Jackson Laboratory	IMSR_JAX:000664
Mouse: B6.FVB(Cg)-Tg(Tlx3-cre)PL56Gsat/Mmucd	MMRRC	MMRRC_041158-UCD
Mouse: B6.FVB(Cg)-Tg(Rbp4-cre)KL100Gsat/Mmucd	MMRRC	MMRRC_037128-UCD
Software and algorithms		
Principal component regression	This paper	https://doi.org/10.5281/zenodo.11304034

(*Continued on next page*)

Continued

REAGENT or RESOURCE	SOURCE	IDENTIFIER
Biophysical simulation of stochastic channel gating	This paper	https://doi.org/10.5281/zenodo.11303742
Prairie view	Bruker	NA
MATLAB (R2018a)	MathWorks	https://www.mathworks.com
Python (3.7)	Python Software Foundation	https://www.python.org/
NEURON (7.6)	Hines and Carnevale[82]	https://neuron.yale.edu/neuron/
ImageJ	Schneider et al.[83]	https://imagej.nih.gov/ij/index.html
Arduino	Arduino	https://www.arduino.cc/
Processing	Processing	https://processing.org/
Kilosort	Pachitariu et al.[84]	https://github.com/cortex-lab/KiloSort
Deeplabcut	Mathis et al.[85]	https://github.com/DeepLabCut/DeepLabCut
Other		
Dynamic clamp board	This paper	https://doi.org/10.5281/zenodo.11303939
Ultima *In Vitro* multiphoton microscope	Bruker Nano	SCR_017142
512 × 512 Spatial Light Modulator	Meadowlark Optics	NA
MaiTai HP	Spectra-physics	NA
InSight X3	Spectra-physics	NA
Prism compressor	Newport	PC-TS-KT
Objective	Nikon	N40X-NIR
Vibratome	Leica	VT1200 S
Multiclamp 700B	Molecular devices	NA
Digidata 1550B	Molecular devices	NA
RHD Recording Controller (512 ch)	Intan technologies	NA
RHD Recording Headstages	Intan technologies	RHD 128ch
Silicon probe	Masmanidis Lab	64D
CCD camera	Teledyne FLIR	Blackfly USB3
Spectral X	Lumincor	NA

RESOURCE AVAILABILITY

Lead contact

Correspondence and requests for materials should be addressed to Dr. Krishna Jayant (kjayant@purdue.edu).

Materials availability

This study did not generate any new materials or unique reagents.

Data and code availability

The datasets generated during the current study are available from the corresponding author upon request. All data analysis and figure generation codes are available on github: https://github.com/shulanx1/SynMultiplex. All code used in the biophysical models is available on GitHub: https://github.com/shulanx1/stochasticH_python. All data and code reported in this paper has been deposited at Zenodo and are publicly available as the date of publication. DOIs are listed in the key resources table. Any additional information required to reanalyze the data reported in this paper is available from the lead contact upon request.

EXPERIMENTAL MODEL AND STUDY PARTICIPANT DETAILS

Animals

All experimental procedures were conducted under the guidelines set forth by the NIH and Purdue Institutional Animal Care and Use Committee (IACUC). Male and female mice were used from the following strains: C57BL/6J (RRID:IMSR_JAX:000664), TIX3-cre (B6.FVB(Cg)-Tg(Tlx3-cre)PL56Gsat/Mmucd, RRID:MMRRC_041158-UCD), Rbp4-cre (B6.FVB(Cg)-Tg(Rbp4-cre)KL100Gsat/Mmucd, RRID:MMRRC_037128-UCD).

METHOD DETAILS

Acute slice preparation

All physiological solutions were fully oxygenated (95% O_2 and 5% CO_2), pH adjusted to 7.3 to 7.4, and osmolarity maintained between 300 and 310 mOsm unless stated. Adult C57BL/6 (Jackson Laboratory, 000664) mice (both male and female, 12 to 24 weeks of age) were deeply anesthetized with 3–4% isoflurane followed by *trans*-cardiac perfusion with ice-cold NMDG cutting solution[86,87] consisting of (in mM): 92 NMDG, 30 $NaHCO_3$, 1.2 NaH_2PO_4, 20 HEPES, 2.5 KCl, 25 glucose, 5 sodium ascorbate, 3 sodium pyruvate, 2 thiourea, 0.5 $CaCl_2$, 10 $MgCl_2$, 5 N-acetyl-L-cysteine, before decapitation. Coronal slices (300 μm–350 μm thickness) were prepared using a vibratome (Leica VT1200S) in 0°–4°C NMDG cutting solution. Brain slices were then allowed to recover in 34°C NMDG cutting solution with gradual spike-in of 0.5–1 mL Na^+ rich NMDG solution (2M NaCl in NMDG cutting solution) over 5 to 10 min (time dependent on mouse age)[87] and transferred to room temperature HEPES artificial cerebrospinal fluid (ACSF) holding solution consisting of (in mM): 92 NaCl, 2.5 KCl, 1.25 NaH_2PO_4, 30 $NaHCO_3$, 20 HEPES, 25 glucose, 5 sodium ascorbate, 3 sodium pyruvate, 2 thiourea, 2 $CaCl_2$, 2 $MgCl_2$, 5 N-acetyl-L-cysteine for at least 1h before recording.

Electrophysiological recording

Slices were transferred to a chamber, continuously perfused with oxygenated ACSF, and visualized with an upright two-photon microscope (Bruker Nano, Madison, WI) comprising of an Olympus BX51WI body (Olympus, Tokyo, Japan) fitted with infra-red (IR) Dodt-gradient-contrast (DGC) optics, an IR sensitive camera (IR-2000, Dage-MTI, Michigan City, IN), and a 40x water immersion objective (0.8 NA, Nikon USA). Recordings were performed in 34°C recording ACSF consisting of (in mM): 125 NaCl, 3 KCl, 25 $NaHCO_3$, 1.25 NaH_2PO_4, 25 glucose, 3 sodium pyruvate, 1 sodium ascorbate, 1.3 $CaCl_2$, 1 $MgCl_2$. 4 to 6 MΩ borosilicate patch pipette (10–15 MΩ for patching apical dendritic trunk) (Sutter Instruments, CA, USA) were pulled using a P1000 pipette puller (Sutter Instruments, Novato, CA), filled with internal solution containing (in mM): 130 potassium gluconate, 7 KCl, 10 HEPES, 5 NaCl, 35 sucrose, 2 $MgSO_4$, 2 sodium pyruvate, 4 Mg-ATP, 0.4 Tris GTP, 7 phosphocreatine disodium (pH 7.3, osmolarity 290mOsm). 25 μM Alexa 594 or 100 μM Alexa 488 was used for two-photon structural imaging, 200 μM fluo-4 was used for two-photon Ca^{2+} imaging. L5 neurons were patch-clamped and had resting membrane potentials between −60 mV and −70 mV at rest without any current injection. Currents of ∼ -50pA to −100 pA was injected when needed to maintain more negative RMP (∼-75mV). Whole-cell recordings were made using a Multiclamp 700B, (Molecular devices, San Jose, CA), Bessel-filtered at 4kHz, and digitized at 4 to 20 kHz using a Digidata 1550B interface (Molecular devices, San Jose, CA) and winwcp software.

Dynamic clamp

A microcontroller-based circuit board[88] was used for performing dynamic clamp experiments. The module was controlled with custom-written codes (Arduino, Processing). First, the linear input-output relationship of the amplification circuit was measured with a DC voltage source (E3631A Agilent Technologies, Santa Clara, CA) and oscilloscope (Keysight, Santa Rosa, CA), and then verified with a model cell (Molecular devices, San Jose, CA). The working principle is as follows: the microcontroller reads the output of the amplifier and then A/D converts the amplified membrane voltage, computes the current based on differential equation models, and D/A converts the current, which is then summed with the current command from the Digidata 1550B interface (Molecular devices, San Jose, CA). The ODEs are solved using the forward Euler method.

The Ornstein-Uhlenbeck process-based point conductance model[89] was used to mimic background synaptic inputs under a noisy *in vivo* like state. We used this point conductance model instead of a Poisson train of synaptic inputs[25] to ensure higher variability in the amplitude of EPSPs and IPSPs, which better reflects the background synaptic inputs with different synaptic strengths. The dynamic conductance is computed with the following differential equations (Equations 1, 2, and 3) (χ_1 and χ_2 are two independent random variables following unit normal distribution),

$$I_{syn}(t) = g_e(t) \cdot (V_m(t) - E_e) + g_i(t) \cdot (V_m(t) - E_i) \quad \text{(Equation 1)}$$

$$\frac{dg_e(t)}{dt} = \frac{\overline{g}_e - g_e(t)}{\tau_e} + \sqrt{D_e} \cdot \chi_1(t), \chi_1 \sim N(0,1) \quad \text{(Equation 2)}$$

$$\frac{dg_i(t)}{dt} = \frac{\overline{g}_i - g_i(t)}{\tau_i} + \sqrt{D_i} \cdot \chi_2(t), \chi_2 \sim N(0,1) \quad \text{(Equation 3)}$$

In our experiment, τ_e = 2.8 ms, τ_i = 8.5 ms, E_e = 0 mV, E_i = −80mV, were chosen based on the physiological properties of α-amino-3-hydroxy-5-methyl-4-isoxazolepropionic acid (AMPA) and γ-Aminobutyric acid (GABA) channels. The mean of noisy excitatory conductance ($\overline{g}_e$) varies between 2 nS to 4 nS for different amount of spontaneous background firing rate, and $\overline{g}_i$ equaled 2nS to 9nS. Conductance values agreed with previous literature and this range helped match the background firing rates to that observed *in vivo* (2–20 Hz), but avoided a hyperexcitable state. The noise diffusion coefficients of the excitatory (D_e) and inhibitory conductance (D_i) were scaled to match voltage fluctuations normally observed *in vivo* (∼5mV RMS). These terms, which contribute to the "noisy" nature of dynamic conductance, were in line with previous literature[89] and this ensured the fast-fluctuations in the background were

preserved. The microcontroller codes and circuit design to realize the dynamic clamp experiments are available from https://github.com/shulanx1/dynamic_clamp.

Simultaneous two photon imaging and 3D holographic glutamate uncaging

Simultaneous two-photon imaging and 3D holographic glutamate uncaging were performed using a laser-scanning microscope (Bruker Nano, Madison, WI) fitted with dual-galvanometric mirrors, a spatial-light-modulator, custom-designed pulse compression and diagnostic measurements, and two femtosecond pulsed lasers (Insight X3 and Mai-Tai, Spectra Physics). Laser beam intensities were independently controlled with electro-optical modulators (model 350-50; Conoptics, USA). A 512*512 spatial light modulator (Meadowlark Optics/Boulder Nonlinear Systems, Lafayette, CO) was coupled to the uncaging path and relayed to the pair of uncaging galvanometers. A half-wave plate was used to achieve the preferred polarization by monitoring the first-order efficiency of the SLM, and a look-up table optimization was performed to maximize the diffraction efficiency at 740 nm. A zero-order beam block was placed at the conjugate image plane. A custom-designed Temporal Dispersion Compensation (TDC) module in conjunction with a Michelson intensity autocorrelator was employed for pulse compression and diagnostic measurements. The TDC arm comprised a dual Prism assembly in folded mirror configuration, and the compressed pulse was then redirected by a pickoff mirror to the Michelson Interferometer for pulse width measurements at the microscope sample plane. The imaging beam (810 nm for Alexa 594 and fluo-4, 920 nm for Alexa 488) and uncaging beam (740nm) were combined using a 760 nm long pass dichroic mirror. During Calcium (Ca^{2+} imaging, line scans were performed across the spine head and the adjacent branch with 8 μs–10 μs dwell time (400–800 Hz line rate) and 3 mW–5 mW laser power at the objective focal plane. Structural imaging was performed at 5 μs–8 μs dwell time. For glutamate uncaging with 4-methoxy-5,7-dinitroindolinyl-L-glutamate trifluoroacetate (DNI-glu-TFA) (Femtonics inc., Budapest, Hungary),[90] 1.5 mM–2 mM DNI-glu-TFA was diluted in freshly prepared recording ACSF and applied to the bath through a circulating pump. At these concentrations, there was no epileptiform-like activity. The uncaging dwell time was 1 ms and the laser power needed for uncaging ranged from 12 mW to 18 mW. At these powers no visible photodamage occurred. Baseline fluorescence of both channels was continuously measured to assay any damage. Ca^{2+} transients were also measured to ensure spines were still functionally active with no loss in physiological response. EPSP time-course and changes in resting membrane potential following repeated stimulation were also assayed as indicators of any photodamage. Although undesired bleed-through of maximally extinct laser power at the sample plane was <1mW, table-top hard shutters were used to avoid exposure and any off-target uncaging. The minimum time required for the SLM to update its phase mask was 3 ms which also set the limit for how fast multiple synaptic clusters spread across different arbors could be stimulated. Ca^{2+} signals were expressed as DF/F (calculated as $(F - F_{baseline})/F_{baseline}$). To estimate the axial beam steering limit of SLM (Figure 1D), we centered a single holographic spot (beamlet) on a spine head of interest and uncaged while gradually defocusing the zeroth order focal plane of the objective axially. Given the maximum power available at the sample plane (~180 mW), we were able to stimulate a maximum of 12 spines in a cluster with high efficiency and up to 36 spines spread across 3 groups along separate dendritic arbors with the only delay being the 3 ms needed between phase masks. Data was collected from dendrites that were at least 30 μm below the surface of the slice that were not prematurely cut off before termination.

PSF estimation of holographic uncaging spots

We experimentally estimated the holographic uncaging resolution of our customized SLM microscope by imaging sub-resolution fluorescent beads (100 nm FluoSpheres, Molecular Probes, USA) embedded in 2% agarose[91] when SLM was engaged. The excitation wavelength of the pulsed laser was set at 800 nm. Serial sections of the sample were performed at a step size of 100nm. Intensity profiles along horizontal and vertical to the image plane through the bead were measured. After subtracting the baseline fluorescence intensity measured from the dark background, the fluorescence intensity was fitted to a Gaussian (Equation 4) (a, b and c are the fitting parameters). The full width at half maximum (FWHM) (Equation 5) was taken as a measure for the optical resolution of the system in lateral and axial dimension respectively (Figure 1A).

$$I(x) = a \cdot exp\left(-\left(\frac{x-b}{c}\right)^2\right) \quad \text{(Equation 4)}$$

$$FWHM = 2\sqrt{ln(2)}c \quad \text{(Equation 5)}$$

Pharmacology

D-AP5 (Tocris, USA) was suspended in water as 50 mM stock solution. Tetrodotoxin (TTX, Tocris, USA) was suspended in 2 mM citric acid as 1mM stock solution and diluted to 1 μM with ACSF on the day of experiment. Recording ACSF containing pharmacological blocker(s) was washed in through the perfusion system. Recordings were performed 5 to 10 min after pharmacological blocker wash-in.

Principal component regression of spike temporal structure

For each spatiotemporal uncaging pattern, 10 repetitive uncaging trials are performed at no more than 1Hz to avoid any plasticity. The uncaging evoked spiking response is first segmented with a 100ms window after uncaging onset time. Then, the spike time is

detected and binned with a 0.1ms window to form a binary spike train with 1000 time points. The binary spike train is convolved with an EPSP-shape kernel as described below (τ_1 = 0.1ms, τ_2 = 2ms). The filtered spike trains (10 repetitive trials for each uncaging pattern) are used to compute correlation matrix and regression analysis.

$$K = dt\frac{-1}{\tau_2} - dt\frac{-1}{\tau_1} \quad \text{(Equation 6)}$$

Principal component regression is performed between any pairs of two different uncaging patterns under the same neuron (Figures 5 and 6), or between uncaging evoked and spontaneous spike trains (Figure S10). To construct the spontaneous spike trains, we first truncate out the 100ms uncaging evoked windows, then concatenate the rest of the traces. Then, we randomly sample 10 windows of 100ms from the spontaneous traces. Then, the sampled trials are processed similarly to the uncaging evoked trials described above. The filtered spike responses can be written as an N×T data matrix $X = [\mathbf{x}_1, \mathbf{x}_2, \ldots, \mathbf{x}_{20}]^T$, with $\mathbf{x}_1$ to $\mathbf{x}_{20}$ being the filtered spike train vector, N being the total number of trials (20, with 10 trials from each pattern), and T being the number of time points (1000). Singular value decomposition is then performed on the data matrix X:

$$X = USV' \quad \text{(Equation 7)}$$

Note that X is an N×T matrix, therefore the columns of V (T×T) form the orthogonal basis for the dimensional decrease of time points. The number of principal components is decided so that the smallest singular value is larger than half of the largest one (2 or 3 principal components most of the cases). The data matrix X is then projected to the principal component space:

$$X_d = X \cdot [\boldsymbol{v_1}, \boldsymbol{v_2}, \ldots \boldsymbol{v_{pc}}] \quad \text{(Equation 8)}$$

Now with X_d being the dimension-decreased data matrix (N×PC) and PC being the number of principle components, each row of X_d is the projection of the filtered spike train onto the principal component space.

We use the linear least square estimator to perform the linear regression. The classifier label Y is assigned as 1 for one of the two patterns, and −1 for another to maintain zero mean (Y = [1, 1, …1, −1, −1, …-1]). X_d and Y are mean-subtracted, and the linear regression weight is computed with the following equation:

$$w_{opt} = \left[X_d^T X_d\right]^{-1} X_d^T Y \quad \text{(Equation 9)}$$

The estimated classifier can be expressed as:

$$\widehat{Y} = X_d w_{opt} \quad \text{(Equation 10)}$$

The R-square value of the linear regression is computed as:

$$R^2 = \frac{1 - |\widehat{Y} - Y|^2}{|Y - \overline{Y}|^2} \quad \text{(Equation 11)}$$

To compute the shuffled baseline, the trials in X are randomly assigned with the classifier label (1 or −1) regardless of the trial types, and the R^2 values are computed as described above. While the data size is relatively small (20 trials), the shuffling is performed 5 times and the average R^2 is used as the baseline R^2 value.

Surgery procedures

C57BL/6 male and female mice were used in approximately equal numbers. Adult mice (between 12 and 24 weeks of age) were used for *in vivo* experimentation. Mice were kept on a 12-h light/dark cycle in conventional housing and had unrestricted access to food and water. Adult C57BL/6 mice were deeply anesthetized with 3–4% isoflurane. Anesthesia was maintained with 1–1.5% isoflurane during surgery with an oxygen flow rate of ∼0.1 L/min. A thermal pad (Kent Scientific) was used during the surgery to maintain the body temperature. Carprofen (5 mg/kg body weight) and dexamethasone (0.6 mg/kg body weight) were injected subcutaneously, and lidocaine was injected under the scalp after the induction of anesthesia. Eye ointment was applied, and the scalp was shaved and sanitized before the incision of the scalp. 3% hydroperoxide is applied on the skull and removed by dry cotton swabs to remove the excessive tissue. For intrinsic imaging, the skull was thinned to a 4 mm diameter to visualize the vasculature under the stereoscope. Vetbond (3M, Saint Paul, MN) was applied to the dried skull surrounding the thinned region. A custom-designed Titanium headplate was glued to the skull with metabond (Parkell, Brentwood, NY). Mice were injected with carprofen Intraperitoneally for up to two days after the surgery. Before silicon probe recording sessions, mice were head-fixed and habituated on a circular running treadmill for 2 sessions (40 min each).

Virus injection

To label L5a pyramidal neurons in S1, adult TIX3-cre mice (41158, MMRRC, 10 to 24 weeks of age) were anesthetized and injected with carprofen and dexamethasone as described above. After sanitizing the scalp, an incision was made on the scalp. AAV1-FLEX-tdTomato (28306, Addgene, Watertown, MA) was injected bilaterally to S1 at stereotaxic coordinate 3.5mm lateral and 1.5mm posterior to bregma, at 500μm and 700μm below pia (250nL per depth, 1E13 GC/mL) with a microinjector (UMP3, WPI, Sarasota, FL), at a

rate of 25 to 50nL per minute. To label L5b pyramidal neurons in S1, retrograde AAV (20298, Addgene) was injected bilaterally in higher-order posterior thalamic nucleus (medial part, Pom, 200 to 500nL, stereotaxic coordinate to bregma: 1.2mm (L), 2.2mm (P), 3mm (V)) in adult Rbp4-cre mice (37128, MMRRC, 10 to 24 weeks of age). The scalp was then sutured and the mouse was recovered from anesthesia. The slicing/immunohistochemistry experiments were performed 3 to 4 weeks post injection.

Intrinsic optical imaging

Mice were head fixed, anesthetized with 3–4% isoflurane, and placed under a CCD camera (Blackfly USB3, Teledyne FLIR) equipped with a focus lens (Nikon, USA). The camera and lens were angled at 10° for a perpendicular visualization of the barrel cortex. Light anesthesia was maintained with 0.5% isoflurane and the oxygen flow rate adjusted to 0.2L/minutes to maintain relatively high respiration rates. This ensured an increase in the oxygenation of hemoglobin and the intrinsic image contrast. A thermo pad was used to maintain the body temperature during anesthesia. Mineral oil was applied along the thinned skull and a coverslip placed on the top to ensure a stable moisture-free image intensity. An image of the vasculature was taken as a reference with green LED illumination. A red LED (lumincor, spectral X) was used to illuminate the thinned scalp for intrinsic imaging. Custom-written MATLAB (MathWorks, Natick, CA) and Arduino codes were used for intrinsic imaging. During each imaging trial, the whisker of interest was deflected with vibration of a hook controlled by a stepper motor, and 100 frames were recorded before and during the whisker deflection at 30Hz. The frames taken before and during whisker deflection were averaged respectively, and the difference between the two averaged images formed the intrinsic optical signal for one trial. The trial was repeated for 6 to 8 times, and the image from each trial was averaged until the contrast of the image was clear and the barrel distinguishable from the background. The image was then contrast-enhanced and smoothed before overlaying on top of the reference image of the vasculature.

In vivo silicon probe recordings

64 channel silicon probes (from Masmanidis Lab in UCLA, 64D) were electroplated (Intan, USA) so that the impedance was lower than 200 kΩ prior to each recording session. After anesthetizing the animal, a burr hole (less than 1mm in diameter) was made with a dental drill on the skull above the target barrel, identified via intrinsic optical imaging. The silicon probe was inserted at an angle of 10° and a speed of 10 μm/s. The mouse was head fixed on a circular running disk while the whisker was brushed with a post controlled by a stepper motor (Wantai motor, China). Treadmill rotation was captured by a rotary encoder (H5-1000-IE-D, US digital). Whisker deflection was performed in 15s intervals, and 200 to 400 trials of whisker deflections were performed across each animal. Whisker motion was recorded via a 45-degree mirror mounted under the treadmill onto a high-speed camera (DR1-D1312IE-200-G2-8, Photonfocus, Lachen, Switzerland) at 250 to 500 fps. The electrophysiological recording was performed with an Intan head stage (RHD2164, Intan Tech., USA) and digitized at 20 kHz. Each whisker deflection trial was truncated from 3s before to 3s after the whisker deflection. The spike sorting of silicon probe recording was performed with kilosort[84] followed by manual clustering. For the local field potential (LFP), the raw data recorded from the silicon probe was filtered with a low pass filter at 500Hz and two notch filter at 120Hz and 60Hz respectively in MATLAB (MathWorks, Natick, CA).

Point-source stochastic Hodgkin-Huxley model

To simulate the probabilistic nature of ion channels, a 13-state discrete Markovian kinetic scheme (8 states for Na^+ channels, 5 states for K^+ channels[59]) was used and incorporated into the Hodgkin-Huxley model (stochastic HH model). This model included 3 identical activation gates (m) and 1 inactivation gate (h) for Na^+ channels, and 4 identical activation gates (n) for K^+ channels. The opening and closing of each binary gate were assumed to be independent and the rate of transitioning between the opening and closing state equals the opening (α) and closing rate (β) in the classic Hodgkin-Huxley model. The transition of ion channels between states can be regarded as a large number of independent random binary events, therefore the number of channels transitioning from state i to state j (Δn_{ij}) within the time duration of Δt can be estimated with random variables that follow the binomial distribution $\Delta n_{ij} \sim binom([n_i], p = A_{ij}dt)$. Here, $[n_i]$ denotes the number of channels currently in state i, and A_{ij} denotes the rate of a single ion channel transiting from state i to j (Figure S4B, noted on the arrows that denotes transition between states). An ion channel is assumed to be conductive only in the state where all the activation gates and the inactivation gate (if applicable) were opened (n_4 state for potassium channels, m_3h_1 state for sodium channels). The total Na^+ and K^+ ionic conductance was estimated with the multiplication of the single-channel conductance and the number of fully activated channels $g_K = \gamma_K * [n_4]$ and $g_{Na} = \gamma_{Na} * [m_3h_1]$, in which γ_K and γ_{Na} denotes the conductance of a single fully conductive ion channel. The following ordinary differential equations (ODEs) (Equations 12, 13, 14, and 15) were used in the simulations:

$$C_m\frac{dV}{dt} = I_{inj} - g_{Na} * (V_m - E_{Na}) - g_K * (V_m - E_K) - g_{leak} * (V_m - E_{leak}) \quad \text{(Equation 12)}$$

$$g_{Na} = \gamma_{Na} * [m_3h_1] \quad \text{(Equation 13)}$$

$$g_K = \gamma_K * [n_4] \quad \text{(Equation 14)}$$

$$\frac{\Delta n_i}{dt} \sim \sum \frac{binom([n_j], p = A_{ji}dt)}{dt} \quad \text{(Equation 15)}$$

The differential equations were solved using the forward Euler method with a time interval (dt) 0.01ms. All the ion channels were at the lowest state (n_0 for K channels and m_0h_0 for Na channels) at initiation, which resulted in less than 5 ms of initialization artifact, a fraction of the 250 ms period per simulation. The total numbers of Na^+ and K^+ channels were 12000 and 3600 respectively, other parameters can be found in Table S1. The simulation was performed using custom-written python code (https://github.com/shulanx1/stochasticHH_python).

Analytical estimation of conductance visibility in the dendrites

Following the method outlined by Koch and colleagues,[63] we estimated the visibility factor of the somatic high conductance state in the basal dendrites. We assumed the dendrites are passive, in which case the visibility factor can then be expressed with:

$$\Gamma = \frac{exp\left(-\frac{2x}{\lambda_{ds}}\right)}{1+\left(1-exp\left(-\frac{x}{\lambda_{ds}}-\frac{x}{\lambda_{sd}}\right)\right)K_{ss}g_s} \quad \text{(Equation 16)}$$

Here, λ_{ds} is the forward propagation (dendrite to soma) space constant, λ_{sd} is the back-propagation space constant, K_{ss} is the somatic input impedance, g_s is the somatic conductance, and x is the distance of the dendrite segment to the soma. When the somatic conductance introduced by the dynamic clamp is relatively lower than the somatic membrane conductance ($K_{ss}g_s \ll 1$), the visibility factor approximately follows the exponential decay, with the space constant about half of the forward propagation space constant ($\frac{\lambda_{ds}}{2}$). Under this condition, the dendritic space constant (λ_{ds}) is the primary determining factor of conductance visibility, suggesting that conductance visibility increases with higher dendritic input impedance. Using results from published experimental findings,[37] the steady state forward propagation space constant was assumed to be 250μm, and the steady state backward space constant was assumed to be 609μm. The somatic resistance was within our experimental range of ~70MOhm, and the average somatic dynamic conductance was 2nS. With these values, the half-decay point of conductance in the dendrite was around 80μm, while the space constant for conductance visibility was ~120μm.

L5 PN sub-type classification

L5a PNs were identified with TIX3-cre injection as described in the virus injection section. L5b PNs were identified with either thick-tufted morphology (lateral span of apical tuft dendrites >150μm) or retrograde tracing as described above. The AP waveforms of spikes (evoked by current injection just above the rhobase) were extracted and normalized to perform cell type inference. A support vector machine (SVM) classifier was trained given the morphologically or genetically identified L5a and L5b PNs (9 identified L5a PNs and 49 identified L5b PNs, data not shown), and was used to identify putative L5a and L5b PNs. The putative regular spiking and intrinsically bursting L5b PNs were subsequently classified based on burst propensity.

QUANTIFICATION AND STATISTICAL ANALYSIS

The structural images were processed with ImageJ, Kalman filtered, and Fourier based filtered when necessary. The Ca^{2+} line-scans signal was preprocessed with a Fourier based narrowband filter to remove line noise when necessary, and the signal fitted with a double exponential curve. No smoothing was performed. Data analysis and statistical tests were performed using custom-written MATLAB (MathWorks, USA) and python code. The spike sorting of silicon probe recording was performed with Kilosort,[84] followed by manual clustering. The whisker tracing was performed with Deeplabcut.[85] Statistical analysis details can be found in the text and figure legends. Unless stated otherwise, the error bars represent mean +/− standard error of mean (SEM).